Article

Photocatalytic 4-Nitrophenol Reduction by Hydrothermally Synthesized Mesoporous Co- and/or Fe-Substituted Aluminophosphates

B. M. Swetha [1,†], Rajeev Kumar [1,2,*,†] , Anupama A. V. [1,3], Sarvesh Kumar [1], Fei Yan [2] and Balaram Sahoo [1,*]

1 Materials Research Centre, Indian Institute of Science, Bengaluru 560012, India; swethabm90@gmail.com (B.M.S.); anupama.av@vidyashilp.edu.in (A.A.V.); sarveshk@iisc.ac.in (S.K.)
2 Department of Chemistry and Biochemistry, North Carolina Central University, Durham, NC 27707, USA; fyan@nccu.edu
3 School of Computational and Data Sciences, Vidyashilp University, Bengaluru 562110, India
* Correspondence: rkumar@nccu.edu (R.K.); bsahoo@iisc.ac.in (B.S.); Tel.: +1-9192256091 (R.K.)
† These authors contributed equally to this work.

Abstract: Mesoporous cobalt- and/or iron-substituted aluminophosphates were synthesized by a hydrothermal method, followed by pyrolysis and calcination. The substitution of the transition metal elements modified the electronic properties of the samples and the accompanying surface characteristics. The samples showed tunable catalytic activity through the substitution of Fe and/or Co. We have demonstrated that the light-induced photocatalytic 4-nitrophenol reduction reaction can be enhanced through the substitution of Fe and/or Co in aluminophosphates. The induction time associated with the three different types of samples, observed due to the influence of the substituents, allows us to understand the mechanism of the 4-nitrophenol reduction process in our samples. Our work solves the issue associated with the origin of induction time and the enhancement of the catalytic activity of mesoporous aluminophosphates in the 4-nitrophenol reduction reaction through a controlled modification of the electronic properties.

Keywords: photocatalysis; induction time; aluminophosphates; transition metal doping; 4-nitrophenol reduction

1. Introduction

Molecular sieves such as zeolites are among the most important industrial heterogeneous catalysts [1–3]. Incorporation of transition metals into mesoporous molecular sieves, viz. silicates, aluminosilicates, and aluminophosphates (APO) has drawn considerable interest for a number of applications due to the tenability in their pore size, specific surface area, and crystallinity [4,5]. The aluminophosphate zeolites have flexible Al–O–P bond angles compared to their analogous Si–O–Si in silicates or Si–O–Al in aluminosilicates, allowing for more morphological tunability. Different transition metal ions have been incorporated into the APO structures [6]. The substitution effects of cobalt and iron in such APO structures have been studied in a few reports [7,8] due to their importance in several applications. For example, iron-substituted aluminophosphate molecular sieves are good redox heterogeneous catalysts [1,9], and cobalt-substituted aluminophosphates are used in heterogeneous oxidation reactions [10]. Although some reports are available on the application of transition metal-substituted APO zeolites, the most necessary understanding of the structure–property correlation is lacking. For instance, to the best of our knowledge, a detailed study on iron–cobalt co-substituted composition incorporated into aluminophosphates, and their catalytic activity is still lacking.

In this work, we synthesized 1.5 mmol of Fe- and/or Co-doped aluminophosphates by a hydrothermal method and studied their structure and other physical properties, along with their catalytic activity towards 4-nitrophenol (NP) reduction. Notably, 4-nitrophenol is

a hazardous organic pollutant often found in wastewater from industries [11]. It has been realized that 4-nitrophenol can be transformed into 4-aminophenol (AP), which is very useful as an intermediate for the manufacturing of many drugs in pharmaceutical companies. However, the conversion of 4-nitrophenol to 4-aminophenol is challenging, even by using the known catalysts. Hence, intensive research work is ongoing to find a good catalyst for an economical conversion of NP to AP [12–15]. In many cases, the NP to AP reduction reaction is demonstrated, which serves as a benchmark reaction for mechanistic studies in catalysis. For example, catalysts such as Au, Ag and Pd nanoparticles [16,17], N-doped graphene-supported Ag nanoparticles [18], metallic and bimetallic sponge dendrites [19], etc., have been tried out. Although the ambient conditions are sufficient to induce a catalytic reaction, most of these particles are either too expensive or not stable for prolonged cyclability. Hence, the search for a suitable catalyst for the reduction of NP to AP and the governing mechanism remains an intense area of research.

Interestingly, our study reveals that the hydrothermally synthesized APO samples often have a thick amorphous semi-transparent coating on their surface, which is detrimental for the catalytic activity of these samples. To improve the catalytic activity of such samples, this covering layer needs to be removed and hence an annealing step at elevated temperatures is necessary. Furthermore, we have demonstrated a temperature-dependent annealing method to control the carbon coating advantageously, thereby protecting the sample from degradation and tuning their porosity and catalytic activity.

In this work, we synthesized four different APO-based zeolite samples, namely $AlPO_4$ (APO), $Co_{0.048}Al_{0.952}PO_4$ (CoAPO), $Fe_{0.07}Al_{0.93}PO_4$ (FeAPO), and $Co_{0.024}Fe_{0.034}Al_{0.942}PO_4$ (CoFeAPO), as well as studied the effect of transition metal (TM) substitution (such as Fe and/or Co) on the physicochemical properties of the APO. In addition to the study of their structure and other physical properties, we demonstrated the usefulness of our Co- and/or Fe-doped APO powder materials for the catalytic conversion of 4-nitrophenol into 4-aminophenol. We demonstrated the enhanced catalytic activity of our samples by using UV–Vis light, and based on our results, a catalytic mechanism has been proposed. Our work also explored the origin of the induction effect in catalysis, which could help in eliminating the limitations of the induction effect while developing catalysts.

2. Results and Discussion

Structure and Properties of Synthesized Samples

The optical photographs of all the synthesized samples are shown in Figure S1 (ESI). The color of the APO-Asp, CoAPO-Asp, FeAPO-Asp, and CoFeAPO-Asp samples were white, bright blue, creamy brown and bluish grey, respectively (first row in Figure S1). These are the respective colors that the corresponding transition metal-based complexes were observed to have. This indicates that our synthesis conditions are suitable for the direct synthesis of transition metal-doped APO samples. After pyrolyzing the samples at 550 °C in Ar atmosphere, all the samples turn blackish, but the Fe-containing samples had a much deeper black color (second row in Figure S1). However, after calcination of the samples at 1000 °C, all the samples attained a deeper color (third and fourth rows in Figure S1) than they were in the as-prepared stage (first row in Figure S1). The changes in color of our samples after different thermal treatments indicate that the particles of the as-prepared samples have a semi-transparent coating on their surface, which transforms to some form of black carbon layer due to pyrolysis at 550 °C in Ar atmosphere, and this black carbon layer burns off after calcination at 1000 °C in air. From the precursors used, we may infer that the semi-transparent coating on the as-prepared samples could be some compounds associated with the acetate-, CTAB-, or isopropoxide-based complex, which later forms the black carbonaceous layer after pyrolysis and burns off after calcination at 1000 °C. We will further discuss these aspects in the following sections.

Figure 1 shows the XRD patterns of all our synthesized samples. In the XRD patterns of any particular set of samples, we observe that the sample calcined at 1000 °C has the highest crystallinity. These crystalline peaks identify the tridymite-type crystal structure (P63mc

space group) [5,8,20,21] of all our zeolite samples calcined at 1000 °C, along with that a small amount of alpha-cristobalite phase that seems to be present [22–24]. Observation of similar peaks in the XRD patterns for the pyrolyzed samples confirms the presence of the same two phases in all the pyrolyzed samples, although the observed crystallinity is not as strong as in the calcined samples. In addition, at the base of the first set of three crystalline peaks, there is a pronounced broad peak observed at $2\theta \approx 26°$, especially for the samples pyrolyzed at 550 °C (in Ar atmosphere). This broad peak could have originated due to the formation of a very defective graphite-like layer on the particle surfaces during the pyrolysis of the samples [25–34]. This aspect will be further understood later. For all the samples calcined at 1000 °C and all the samples pyrolyzed at 550 °C, a broad peak is observed at $2\theta \approx 12°$, which is well pronounced in the XRD patterns of all the samples pyrolyzed at 550 °C. The broad peak, at $2\theta \approx 12°$, can be assigned to the (002) Bragg peak of graphene oxide (GO) [35–37]. The origin of this peak can be understood as follows.
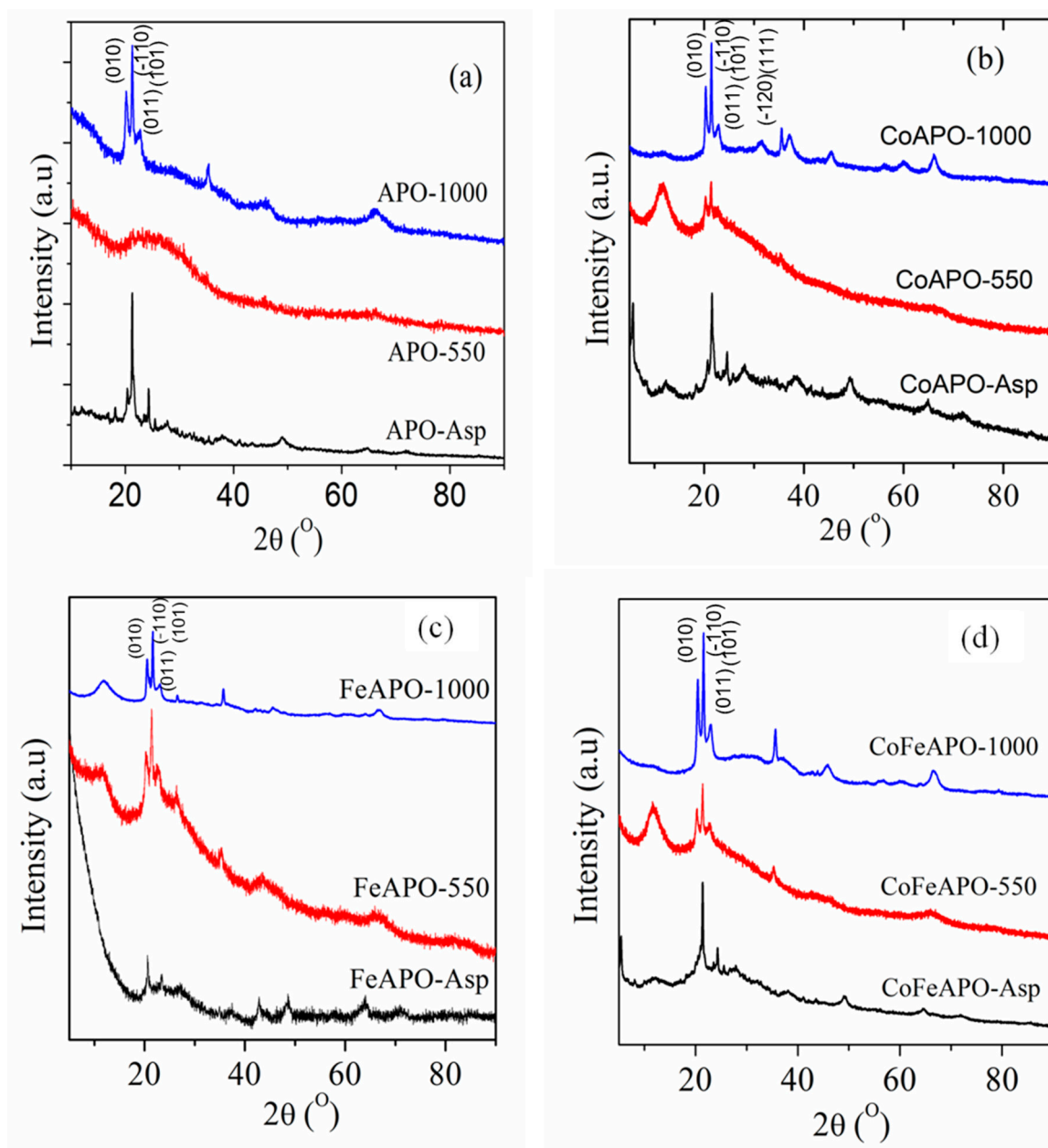

Figure 1. The XRD patterns of the (**a**) APO, (**b**) CoAPO, (**c**) FeAPO, and (**d**) CoFeAPO samples, as indicated.

In the XRD patterns of all the as-prepared samples, in addition to many unidentified small peaks, a sharp peak at $2\theta \approx 21.3°$ corresponding to the (110) Bragg peak of the tridymite-type phase is observed, along with its broad base. This indicates that, interestingly, the intended zeolite phase is formed in all the as-prepared samples. Furthermore, the peak at $2\theta \approx 12°$, observed for the pyrolyzed samples and the calcined samples, is not well pronounced for these as-prepared samples. This indicates that there are some amorphous precursors or reaction intermediates (related to the isopropoxide, acetate and/or CTAB) present on the surface of the as-prepared samples, which are transparent but acts as the carbon source for the formation of the observed graphitic and GO layers after pyrolysis at 550 °C in Ar atmosphere [33,38]. Furthermore, it is clear from the photographs of the samples (Figure S1) that there is no opaque coating (such as graphitic carbon or GO) observed on the as-prepared samples, but there could be a coating of the precursor materials (as discussed above). This coating seems to be relatively thick (thicker than the GO layer of the pyrolyzed samples) but transparent to the visible light; hence, the colors of the zeolite particles (in the as-prepared samples) are clearly visible through this coating (Figure S1, first row). When the samples are pyrolyzed at 550 °C in Ar atmosphere, these coating materials start to form a thick graphene oxide (GO) type of layer, covering the immediate surface of the particles. It should be noted that for pyrolysis, we used Ar atmosphere; hence, the pyrolysis of acetate and/or isopropoxide should lead to a graphitic cover layer on the particles [30,33]. However, observation of GO peaks in the XRD patterns suggests that the pyrolysis temperature was slightly lower than that what is previously generally used [32,33,39]. Hence, the oxygen of the acetate and isopropoxide do not dissociate completely and go away but helps in the formation of the defective carbon layer on the immediate surface of the particles. In addition, partial dissociation of the oxygen functional groups due to pyrolysis also forms a GO-like top cover layer on the particles above the carbon layer. This can be rationalized from the observed broad peak at $2\theta \approx 26°$ in the XRD patterns of the pyrolyzed samples. This aspect can be further clarified from the electron microscopy study later. Hence, the presence of both GO and defected graphitic coating on the top of the particles emphasizes the black color of the samples after pyrolysis, as seen in Figure S1.

Now, for the samples after calcination at 1000 °C in air, this graphitic layer and the GO layers observed for the pyrolyzed samples burn (oxidize) and evaporate. The original color of the samples is exposed again, as shown in Figure S1 (bottom row), i.e., the calcined sample is shinier and deeper in color than the as-prepared samples (where the colors were dull, Figure S1). This dull color of the as-prepared samples, along with the formation of the GO and graphitic layers after pyrolysis, proves the presence of semi-transparent carbonaceous compounds on the surface of the as-prepared samples. Furthermore, a small peak at $2\theta \approx 12°$ corresponding to GO is still present in the XRD patterns of the calcined samples, even after calcination of the pyrolyzed samples at 1000 °C in air. It will be clear from the SEM study later that the observed small GO and graphitic peaks can originate from the bound carbon atoms trapped within the particle boundaries and are gradually released after calcination at 1000 °C. Furthermore, comparing this peak (at $2\theta \approx 12°$) (with respect to the crystalline zeolite peaks) for all the 1000 °C calcined samples, it is clear that the FeAPO sample still has this peak stronger than that of Co samples. This observation is quite interesting, and we will discuss it in the following sections.

To better understand the nature of the coating layer of different samples, let us compare the XRD patterns of the samples synthesized under the same experimental conditions. Careful observation of the XRD patterns of the as-prepared samples reveals that there is a weakly developed broad peak at a 2θ value (>12°), slightly higher than the corresponding peak of GO (seen in the pyrolyzed samples). This indicates that this peak does not correspond to the presence/formation of GO on the particles, but rather the zeolite particles are covered by a few layers of the precursor-derived material. Among the as-prepared samples, the XRD peak of the cover layer (at 12°) is more pronounced for the CoAPO-Asp sample and least pronounced for the FeAPO-Asp sample. This suggests that the samples

having Co as dopants (CoAPO) have a higher tendency to form a coating of striated nature than samples with Fe dopants (FeAPO). Hence, it can be considered that the materials derived from the carbonaceous precursor are randomly chemisorbed/absorbed inside the FeAPO particles; correspondingly, a high background is observed at lower Bragg angles. Simultaneously, a high background is observed for the FeAPO-550 sample, in comparison to the other pyrolyzed samples. This indicates that there is a high amount of amorphous carbon present on the FeAPO-550 sample, along with the GO and graphitic layer on the core zeolite particles. Note here that, as the pyrolysis is performed in the inert Ar atmosphere, the carbonaceous precursor-derived coating of the as-prepared samples would only decompose and form the GO layer on the zeolite core particles [28,40–42]. However, unlike in pyrolysis, calcination at 1000 °C in air would lead to the burning of the GO and graphitic cover layer on the particle surface. Hence, in all the pyrolyzed samples, the intensity of the XRD peaks corresponding to GO and graphite is drastically reduced. However, it can be understood from the XRD patterns that, among all the samples calcined at 1000 °C in air, the FeAPO-1000 sample still shows a relatively higher amount of GO layer on the particles in comparison to the other two samples. Hence, the order of the samples with increasing GO amount is CoAPO-1000 < CoFeAPO-1000 < FeAPO-1000. Therefore, we may conclude that Fe has a stronger affinity to bind with carbon and it does not allow the carbon to be easily burnt. This tendency was also observed earlier in the synthesis of carbonaceous materials by pyrolysis [38,42]. Here, we understand that Fe and C form strong bonds of more covalent character than Co and C, due to better valence electron (electro-negativity) match; hence, Fe atoms trap more C atoms with it. This was confirmed earlier [43] and is also confirmed here from the XRD pattern of the APO-1000 sample.

As mentioned earlier, the intensity of the broad peaks at 12° and 26° in the XRD patterns, corresponding to GO and graphitic layers, are almost burnt off after calcination at 1000 °C in air. The remaining GO layer is very thin. Hence, it can be envisaged that these carbonaceous layers on the zeolite core particles would help in protecting the particles against degradation and from chemical and thermal corrosion [35–37]; however, the surface activity and other physical properties of the core zeolite particles will be shielded. To prove these aspects, we have performed a catalytic activity study of our samples for the reduction of NP to AP, which will be discussed later.

To confirm that the (Fe and Co) dopants are doped in the structure of our zeolite samples, we have compared the peak positions of the tridymite phase in the XRD patterns of the calcined samples, as shown in Figure 2. Clearly, the position of the Bragg peaks shifts as the size of the Fe atoms are smaller than the Co atoms. We have also performed the Rietveld refinement of the XRD patterns of different samples, considering only the tridymite phase only. The least-squares fitted XRD patterns (Rietveld refinement) is given in Figure S2 (ESI) and the refined lattice parameters and the fitting parameters are listed in Table S1 (ESI). The crystallite sizes calculated from Scherrer's equation were found to be 27, 32, 32, and 29 nm (±2 nm) for the APO-1000, CoAPO-1000, FeAPO-1000 and CoFeAPO-1000 samples, respectively.

The SEM micrographs in Figure 3 show the morphology of our synthesized samples. All the samples contain irregularly shaped particles. The particles found in the Fe- and FeCo-doped as-prepared zeolite samples are bigger than that of the CoAPO-Asp sample. After pyrolysis at 550 °C, the size of the particles seems much bigger than those found in the as-prepared samples. This observation is in line with our XRD results that during pyrolysis, the precursor-derived carbonaceous materials decompose to form GO and graphitic layers and the amorphous carbon matrix; during this process, many small particles fuse together through their amorphous carbonaceous cover layer. Furthermore, calcination at 1000 °C, this graphitic and GO cover layer burns off and the particles become separated again. Hence, we have observed many smaller particles in the SEM images of the samples calcined at 1000 °C. Importantly, comparing among the SEM images of, especially, the pyrolyzed samples, one can rationalize that the particles found in the Fe- and FeCo-doped pyrolyzed samples (FeAPO-550 and FeCoAPO-asp) are much bigger than that of the Co-doped

pyrolyzed sample (CoAPO-550). This bigger size is due to the aggregation of the zeolite particles through the fusion of the carbonaceous cover layers, which is mostly amorphous in nature, as observed in the background of the XRD patterns in Figure 1. After calcination at 1000 °C, it seems still some GO layer is present, as particles still seem to be fused through their carbonaceous coating, as will be clear from the TEM results given below.
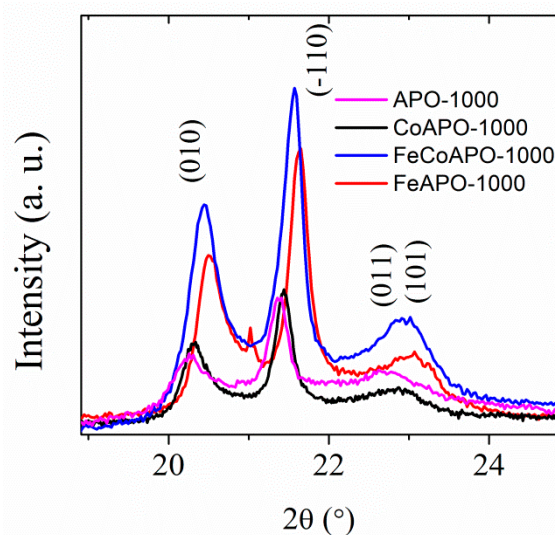

Figure 2. The XRD patterns of the calcined samples showing a comparison between the peak positions for the samples after calcination at 1000 °C in air.

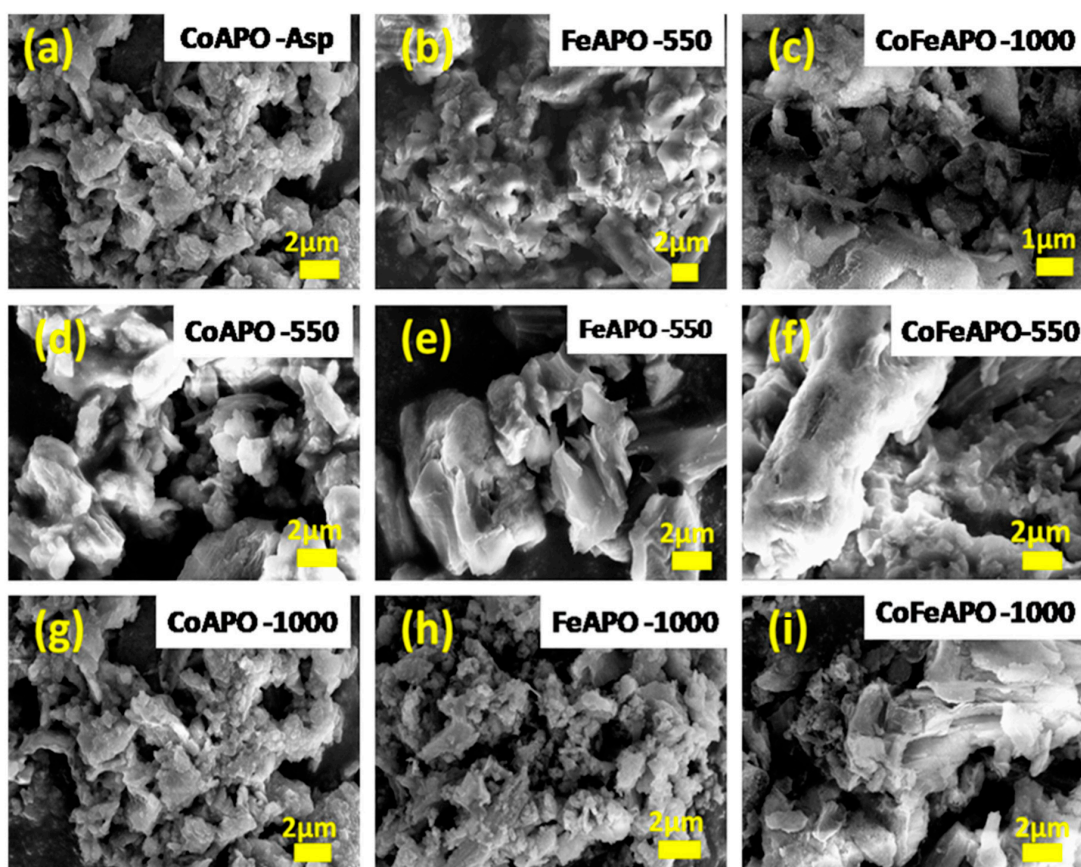**Figure 3.** SEM micrographs of: Top panel: (**a**) CoAPO-asp, (**b**) FeAPO-asp, (**c**) CoFeAPO-asp. Middle panel: (**d**) CoAPO-550, (**e**) FeAPO-550, (**f**) CoFeAPO-550 samples. Bottom panel: (**g**) CoAPO-1000, (**h**) FeAPO-1000, (**i**) CoFeAPO-1000 samples.

The TEM micrographs of pyrolyzed and calcined samples are shown in Figure 4. In all the samples, the core zeolite particles are of long rice/needle-shaped and are connected with each other by the carbonaceous matrix. As explained above, the carbonaceous (GO, graphite, and amorphous carbon) materials are more in pyrolyzed samples, which well separates the rice-shaped zeolite particles than that which was observed in the calcined samples. Among the pyrolyzed samples, the separation between the rice-shaped particles is more for FeAPO-550 and FeCoAPO-550 samples than the CoAPO-550 sample. The calcination of the samples at 1000 °C facilitates burning of the carbonaceous layer and allows the zeolite particles to fuse/connect together, as observed in the TEM images. The high-resolution TEM images of the calcined samples are shown in Figure S3 (ESI). Clearly, as observed in the XRD patterns, the CoAPO-1000 and CoFeAPO-1000 samples show a clear atomic arrangement of the atomic planes.
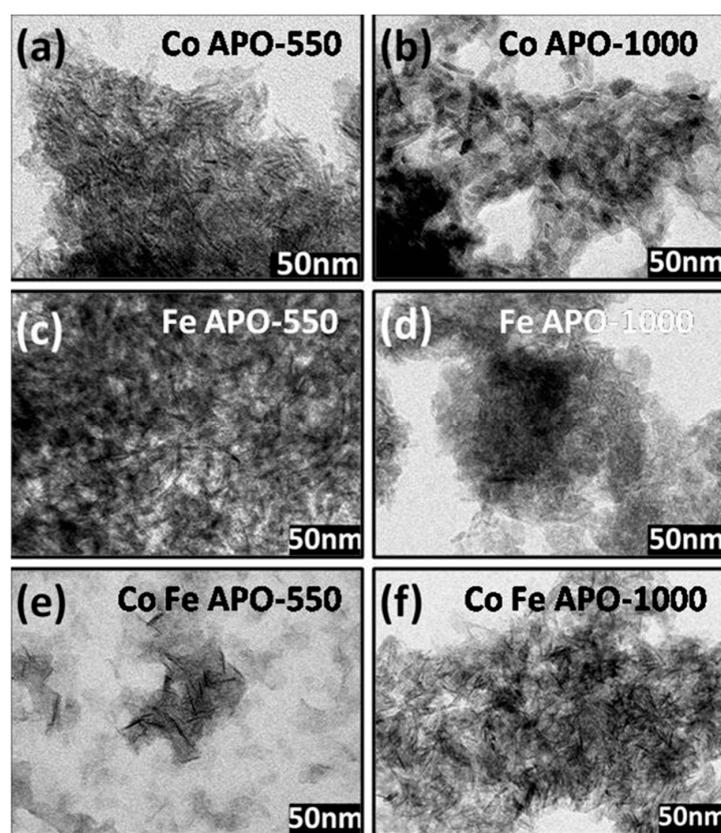

Figure 4. (i) Left panel: TEM images of (**a**) CoAPO-550, (**c**) FeAPO-550, and (**e**) CoFeAPO-550 samples. (ii) Middle panel: TEM images of (**b**) CoAPO-1000, (**d**) FeAPO-1000, and (**f**) CoFeAPO-1000 samples.

In order to understand the structure of our samples better, we performed thermo-gravimetric analysis, TGA. The measured TGA curves for all our samples are shown in Figure 5. All curves show about 5–10% weight loss at lower temperatures, below ~180 °C, associated with the evaporation of the adsorbed gaseous moieties and moisture. Figure 5a shows the TGA plots for all the as-synthesized samples, where we observed a sharp weight loss of about 50–60% at about 250 °C. This low-temperature weight loss suggests that the cover layer consists of precursor-derived carbonaceous moieties, which are then burned off, confirming our previous assumption. Hence, the cover layer of the as-prepared zeolite particles is not GO or graphite but some precursor derived material that works as the carbon source for the formation of GO and graphite layer during pyrolysis. The gradual weight loss for the FeAPO-asp sample confirms the affinity of Fe to keep-bonded with the carbon, as discussed earlier. Figure 5b shows the TGA curves for all our samples obtained after pyrolysis at 550 °C in Ar atmosphere. Here, the weight loss of ~21% at about 500 °C for the FeAPO-550 sample is the maximum among all the pyrolyzed samples, followed by

CoFeAPO-550 and CoAPO-550 (Table S2, ESI). This further emphasizes the affinity of Fe to form a carbonaceous layer around it. Note that this weight loss occurs through the burning of carbon layers (GO and graphite) covering the core zeolite particles in air. Figure 5c shows the TGA curves of all the samples calcined at 1000 °C in air. The weight loss observed at below 180 °C corresponds to the evaporation of moisture and adsorbed moieties. As the carbon layer is burnt during calcination, these samples do not show any major weight loss. However, a weight loss of ~1% is observed above ~800 °C. This is quite interesting and confirms our previous supposition that there are some carbon species trapped between two fused particles which are slowly getting released at higher temperatures. Although it is within the error bar, this weight loss (at ~800 °C) is the highest for the FeAPO-1000 sample (Table S2, ESI).
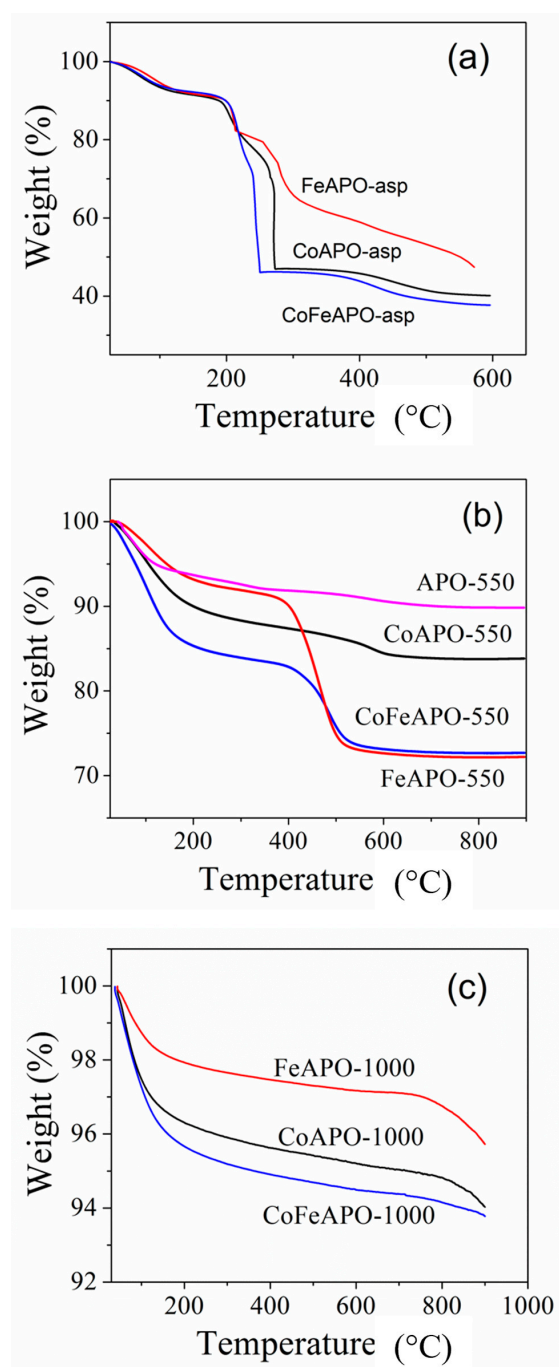

Figure 5. TGA plots of (**a**) As-prepared, (**b**) pyrolyzed (at 550 °C in Ar), and (**c**) calcined (1000 °C in air) samples. Note that the TGA experiments were performed in air atmosphere.

To understand the oxidation state of iron in the zeolite structure, we performed ^{57}Fe Mössbauer spectroscopy at RT. The measured Mössbauer spectra for the FeAPO-1000 and CoFeAPO-1000 samples are shown in Figure 6. The spectra are least-squares fitted by assuming a doublet corresponding to Fe at the Al position. The obtained Mössbauer parameters are listed in Table 1. The presence of a doublet with small isomer shift values (δ = 0.16 mm/s and 0.18 mm/s) for both the samples suggests the presence of trivalent iron in both of our samples. However, the weakly asymmetric shape of the Mössbauer lines suggests the presence of a minute amount of Fe^{+2} state ions. Similar results were earlier observed for the Fe-doped APO zeolite [44] and the Fe-doped yttrium aluminum garnet [45–47].
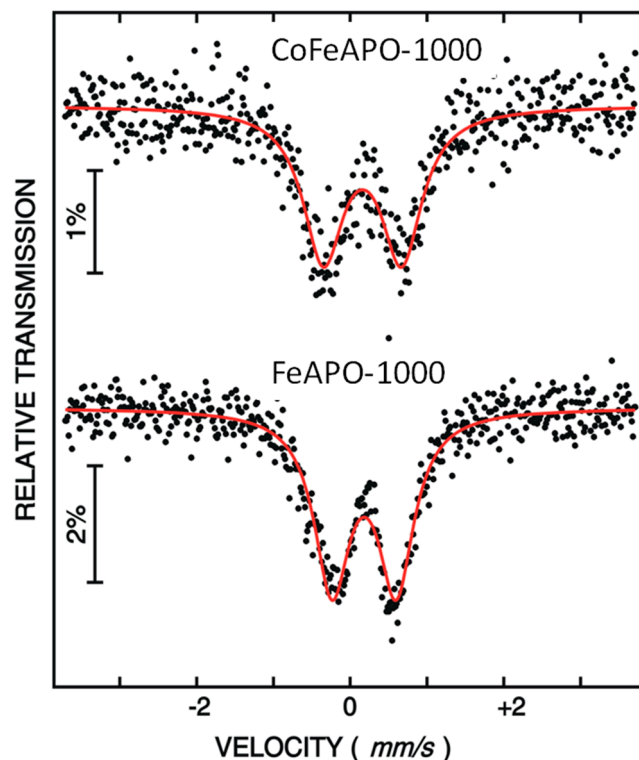

Figure 6. Mössbauer spectra of FeAPO-1000 and CoFeAPO-1000 samples. The black dots are the experimental data points and the red lines are the least square fits.

Table 1. The Mössbauer parameters obtained after fitting the Mössbauer spectra of FeAPO-1000 and CoFeAPO-1000 samples. The isomer shifts are given with respect to the ^{57}Co-source (Rh-matrix) at RT.

Sample	Isomer Shift (δ) (mm/s)	Quadrupole Splitting (Δ) (mm/s)	Peak Line Width (Γ)
Fe-APO-1000	0.180	0.835	0.564
CoFe-APO-1000	0.160	1.018	0.641

Figure 7 shows the XPS spectra of our CoAPO-1000 sample, which helps us to understand the oxidation state of Co, when doped in the APO structure. From the spectrum, it is clear that Co exists in both the Co^{2+} and Co^{3+} states [48–53]. As the oxidation state of the Co (2+) is different from that of Al (3+), there should be some defects/vacancies associated with the structure of Co-doped APO samples. The XPS spectra of FeAPO-1000 and CoFeAPO-1000 have substantial noise and low-intensity peaks (Figure S4, ESI).

The optical properties of zeolites are not often thoroughly explored. However, our samples show very interesting absorption behaviors, as discussed below. The UV–Vis DRS spectra of our samples are shown in Figure 8. Figure 8a shows the DRS spectra of the samples after pyrolysis at 550 °C. As discussed above, under the TEM and XRD results, these samples have a shell of GO and graphitic carbon on the zeolite core particles and are

present inside the amorphous carbon matrix. These carbonaceous layers generally absorb light and appear black, as seen in Figure S1. Hence, a very small reflectance of 15–20% (high absorption) is observed for all the pyrolyzed samples. Interestingly, we observed exciting optical behavior for the samples calcined at 1000 °C in air, as shown in Figure 8b.
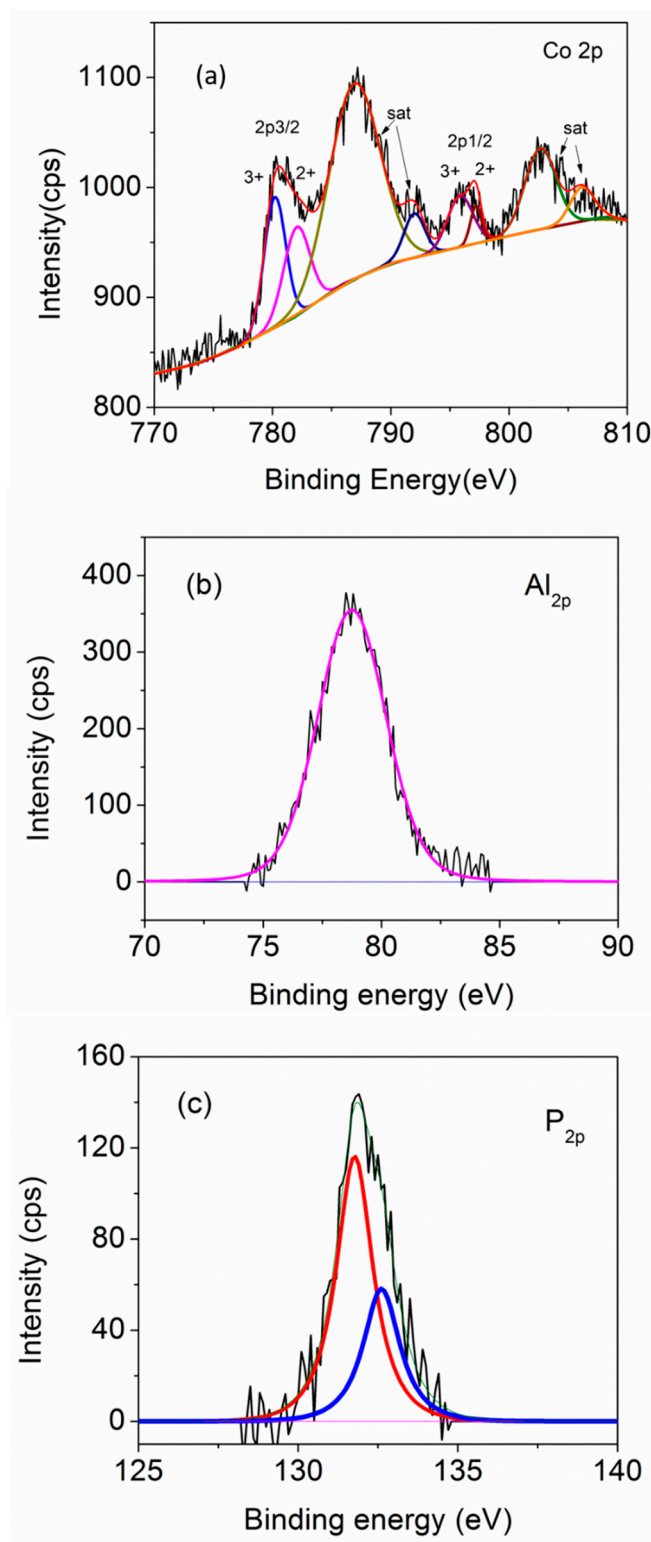

Figure 7. XPS spectra of CoAPO-1000 sample: (**a**) Co-2p edge, (**b**) Al-2p edge, and (**c**) P-2p edge. The black lines are experimental data and colored lines are the sub-fits corresponding to different oxidation states.
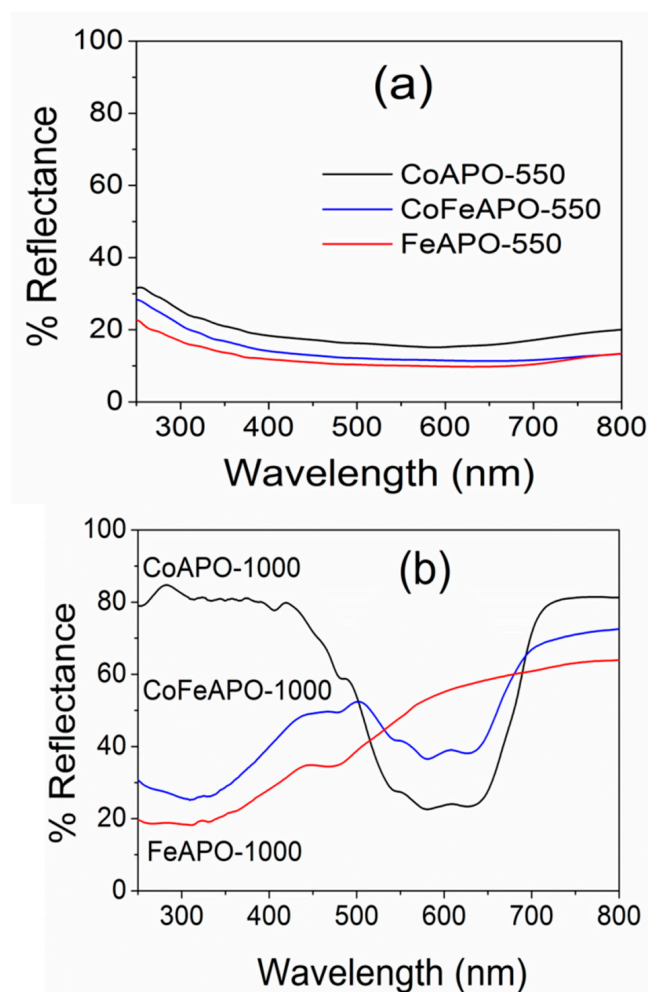
Figure 8. UV–Vis DRS spectra of CoAPO, FeAPO, and CoFeAPO samples (**a**) pyrolyzed at 550 °C in Ar atmosphere and (**b**) calcined at 1000 °C in air.

The maximum percentage of reflectance observed for the FeAPO-1000, CoFeAPO-1000, CoAPO-1000 samples are about 65%, 75%, and 80%, respectively. This variation seems to be associated with the thickness of the GO layer present on the sample surface, as discussed under the XRD results. Although this GO layer is a little detrimental for the optical behavior of the sample, it works as a good shield against corrosion and degradation of the particles [35,36]. In addition, this sample can potentially have high microwave absorption due to their similarity with many other materials used in microwave absorption [46,54,55]. Furthermore, the CoAPO-1000 sample shows lower reflectance only in a small window of wavelengths, ~450–700 nm. This highlights the importance of this sample for its use in optical filter applications, such as a UV filter in smart windows [56,57]. For the FeAPO-1000 sample, the reflectance gradually decreases from 600 nm to 350 nm. However, for the CoFeAPO-1000 sample, a well-defined absorption window of wavelengths is induced. This suggests that by Co and Fe co-doping, the absorption window can be tuned for many potential applications of such materials.

To explore the optical properties of our samples further, we determined the bandgap (Figure 9a–c) of the samples by using Kubelka–Munk formalism [43,58,59]. The values of the bandgaps are listed in Table 2. The bandgaps observed for the pyrolyzed samples are between 1.4 and 1.5 eV, which are often observed for carbonaceous materials [30,32,34]. Hence, this is associated with the carbonaceous layer on the zeolite cores, but not associated with the core zeolite phase. However, as expected, a clear optical absorption window between 1.85 eV and 2.5 eV is observed for the CoAPO-1000 sample, as shown in Figure 9d. The FeAPO-1000 and CoFeAPO-1000 samples show similar band gaps of 3.05 eV and 3.11eV,

respectively. In addition, a clear window of absorption is also featured between 1.8 and 2.5 eV, as shown in Figure 9f. Hence, our materials are useful for advanced applications such as optical filters in smart windows.
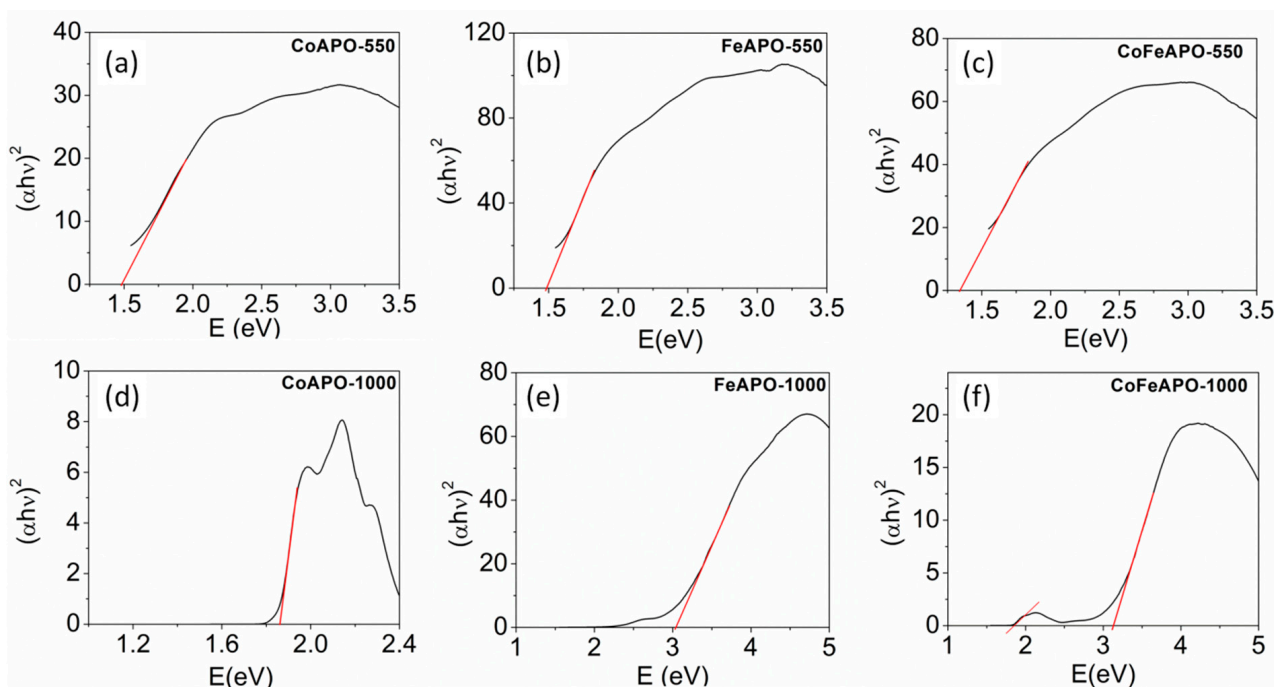

Figure 9. The plot of Kubelka–Munk function, (F(R)hυ) versus hυ, for determining bandgap of our samples: (**a**–**c**) pyrolyzed at 550 °C in Ar atmosphere and (**d**–**f**) calcined at 1000 °C in air.

Table 2. List of bandgaps derived from the Kubelka–Munk plots for the pyrolyzed and calcined samples. * Pertains to the observation of band gaps in two different linear regimes in Figure 9f.

Sample Name	Pyrolyzed at 550 °C	Calcined at 1000 °C
	Band Gap (eV)	Band Gap (eV)
CoAPO	1.47	1.86
FeAPO	1.48	3.04
CoFeAPO	1.34	3.13(1.84) *

To understand the catalytic activity of our samples, knowledge of the surface area exposed to the reactants is very important. The surface of the catalysts is the host ground for the reactants to undergo a reaction. Without the catalysts, the reaction may not proceed. Furthermore, the pore size of our mesoporous zeolite samples can play an important role in their application. For this purpose, we have measured the specific surface area and pore diameters of our samples through nitrogen adsorption–desorption isotherms at 77 K. The nitrogen (N_2) adsorption behavior at 77 K for the CoAPO samples synthesized at different conditions are shown in Figure 10a,b. It is clear that the nature of most of the adsorption–desorption isotherms belong to that of the Type IV isotherms, where a monolayer of the adsorbates is initially adsorbed to the surface of the adsorbent at a low pressure, followed by multilayer formation at a higher pressure, and upon desorption of the gasses, a hysteresis is formed. Hence, the heat of monolayer formation (E1) is higher than the heat of liquification and thus a monolayer forms first. However, the only exception is for the CoAPO-asp sample.

Figure 10a–i shows the adsorption–desorption isotherm for the CoAPO-asp sample. The nature of the isotherm suggests that there is almost no adsorption of the gases in the low-pressure region; however, as the pressure increases, only a marginal volume of gases is gradually adsorbed. The desorption profiles form a hysteresis, making a Type-V-

like adsorption–desorption (isotherm) profile and an H4 type of hysteresis. Hence, there are almost no micropores (<2 nm diameter) present on the surface of this as-prepared (CoAPO-asp) sample.
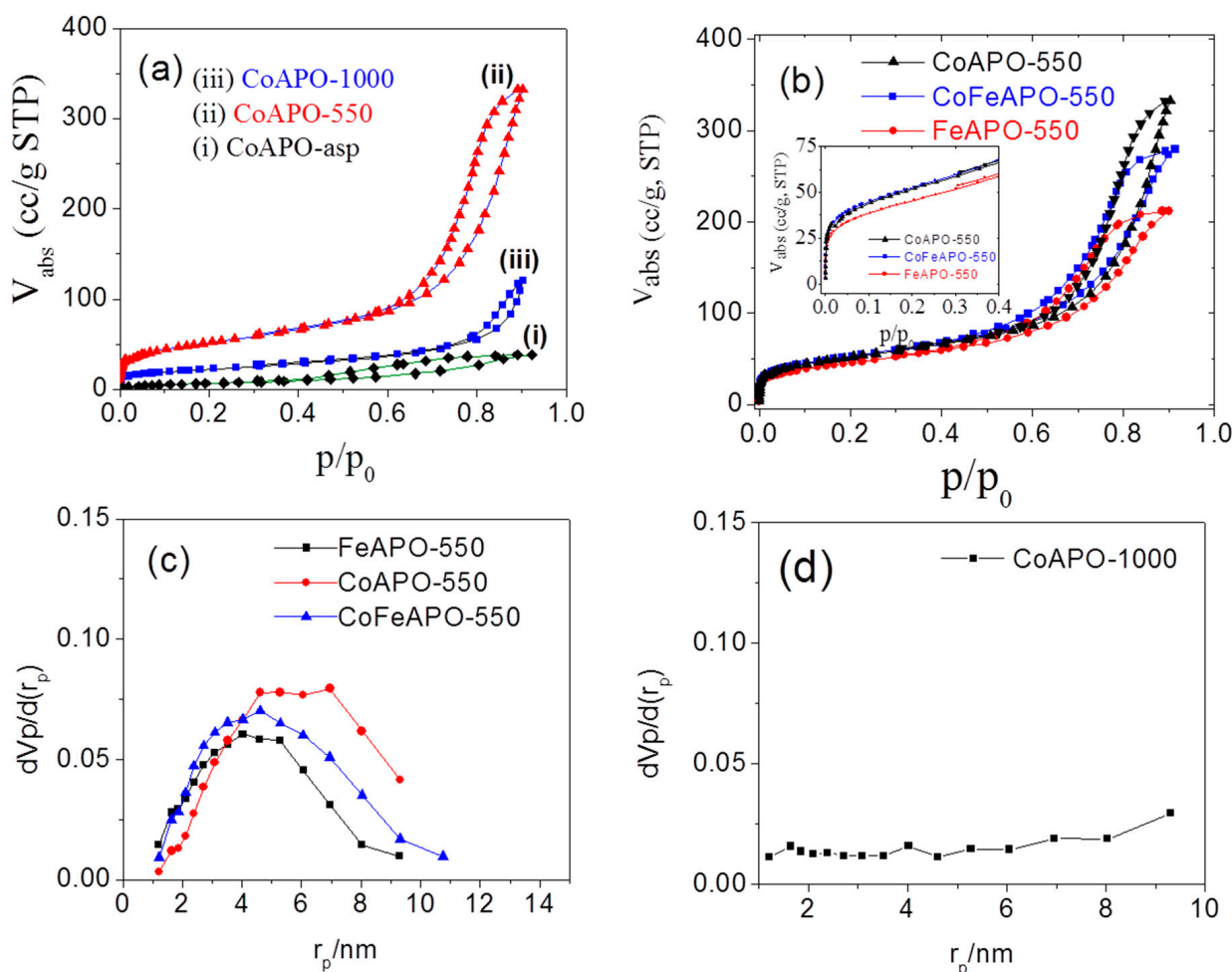

Figure 10. The adsorption–desorption isotherms for the (**a**) CoAPO-asp, CoAPO-550 and CoAPO-1000 samples, and (**b**) CoAPO-550, CoFeAPO-550 and FeAPO-550 samples. BJH analysis plots for (**c**) all the samples after pyrolysis at 550 °C and (**d**) the CoAPO-1000 sample.

Furthermore, with increasing pressure, the multilayers do not form efficiently in comparison to the other CoAPO samples. Hence, it clarifies that the surface materials are different from those of the other samples. There are almost no micropores and the surface coating on the zeolite core particles are very dense (less porous) with a very small amount of mesopores. Capillary condensation of N_2 in these pores leads to the observed horizontal hysteresis. The above observations support our conclusion from the XRD results and the photographs (Figure S1) that the surface of the as-prepared samples has a less-defective (dense) semi-transparent amorphous layer of the precursor-derived (acetate and isopropoxide based) materials.

For the CoAPO-550 sample, a BET-type of adsorption profile is observed (Figure 10a-ii). The Langmuir-type nature of the adsorption isotherm at the low-pressure region suggests that, first, there is a monolayer formation on the surface of the particles, followed by a sharp increase in adsorption, exhibiting a multilayer formation with increasing pressure, and a sharp desorption profile is subsequently observed during a decrease in pressure, forming a Type IV adsorption–desorption isotherm and an H1 type of hysteresis. This hysteresis suggests that there is a pore condensation or capillary condensation process occurring, which implies that there are plenty of pores on the surface of this sample. This

observation clearly explains the nature of the GO and the graphitic layer, which forms due to pyrolysis of the samples, especially the pyrolysis of the precursor-derived layer present on the zeolite core. This feature is often observed in the isotherms of mesoporous carbon [60–62], resembling the nature of the surface of our samples. After calcination of the sample at 1000 °C, the carbonaceous cover layer burns out (as observed in our TGA results). The adsorption–desorption isotherm for our CoAPO-1000 sample is shown in Figure 10a-iii. The low-pressure region of this isotherm is similar to that of a Type-I-like isotherm and is similar to that of the CoAPO-550 sample, but the N_2 adsorption volume is much lower. Hence, the surface area exposed to the monolayer formation is much less. This happens due to the burning of the GO and graphitic layers. This reveals the fact that in the CoAPO-550 sample, the pores were present in the carbonaceous layer on the zeolite particles. Calcination at 1000 °C burns off this carbonaceous layer and the pores would then vanished. Furthermore, for the CoAPO-1000 sample, the multilayer started forming at a higher pressure than what was required for the CoAPO-550 sample, suggesting that the surface of the zeolite core is almost exposed for this sample and the natural color of the sample is also exposed (Figure S1). Our observation suggests that the CoAPO-550 sample exposes high surface area and, as will be made clear later, this sample shows high catalytic activity. In order to explore the influence of the dopants on the formation of this carbonaceous layer and their catalytic activity, other similar samples pyrolyzed at 550 °C in Ar atmosphere were also examined by their adsorption–desorption isotherms.

Figure 10b shows the adsorption–desorption isotherm for all the samples pyrolyzed at 550 °C. All the samples show similar behavior in low-pressure regions, indicating a similar process of monolayer formation. The multilayer formation also starts at a higher but similar pressure range for all the samples. Hence, the characteristics of the pores present in all the samples are similar, i.e., the mean pore diameters for different samples are not very different. However, from the adsorption volume closer to saturation pressure (Figure 10b), it suggests that the specific surface area (S), total pore volume (V_p), and volume of the adsorbate forming a monolayer (V_m) on the adsorbent surface are different. To quantify these parameters, we have analyzed the data using the Brunauer–Emmett–Teller (BET) theory of surface adsorption.

The obtained parameters are listed in Table 3. Clearly, all parameters, S, V_p, and V_m are high for the Co-doped samples pyrolyzed at 550 °C, i.e., the CoAPO-550 and CoFeAPO-550 samples. To obtain the distributor pore volume (pore volume for different pore diameter), we have used the Barrett–Joyner–Halenda (BJH) analysis method. The pore size distribution with pore radius for the pyrolyzed samples is shown in Figure 10c, and for the CoAPO-1000 sample, it is shown in Figure 10d.

Table 3. The surface parameters derived from the adsorption–desorption isotherms by the BET method.

Sample	Specific Surface Area (m²/g)	Total Pore Volume (cm³/g)	V_m (cm³/g, (STP))	Mean Pore Diameter (nm)
CoAPO-asp	26.3	0.06	6.04	8.99
CoAPO-550	168.9	0.51	38.82	12.17
FeAPO-550	152.9	0.33	35.14	8.57
CoFeAPO-550	171.1	0.43	39.31	10.11
CoAPO-1000	72.8	0.19	16.73	10.19

The pore volume, specific surface area, and peak value of the pore radius are listed in Table 4. From Figure 10c, it is clear that the pore size (radius) varies between 1.7 nm and 12 nm. According to the IUPAC definition, most of the observed pores are mesopores (2 nm < r_p < 50 nm). Furthermore, the peak pore radius for all the three samples is not very different, but the pore volume is the highest for the CoAPO-550 sample. Hence, the active surface for this sample is the highest. Figure 10d suggests that the mesopores observed in the pyrolyzed samples vanish after calcination of the pyrolyzed samples. This observation is consistent with all other characterization results that the mesopores observed in the pyrolyzed samples are present in the GO and graphitic coating layers.

The adsorption–desorption behavior analysis of our samples suggests that by our synthesis method, mesoporous carbonaceous materials coated on zeolite surfaces could be synthesized for many different applications. Our studies on the catalytic activities of the synthesized samples are discussed below.

Table 4. The pore volume (V_p), specific surface area (S_p), and the peak value of the pore radius (r_p) obtained from BJH analysis of the adsorption isotherms of the analyzed samples.

Sample	V_p (cm^3/g)	S_p (m^2/g)	r_p (nm)
CoAPO-as	0.0624	0.0359	2.39
CoAPO-550	0.4919	0.1930	6.96
FeAPO-550	0.3170	0.1663	4.02
CoFeAPO-550	0.4218	0.1956	4.60
CoAPO-1000	0.1553	0.0070	9.30

3. Photo-Catalytic Activity of the TM-APO Samples for 4-Nitrophenol Reduction

Mesoporous molecular sieves have been considered in the field of catalysis in recent years because of their high surface area associated with the mesopores. However, owing to the poor catalytic performance, the use of aluminophosphates in the reduction of 4-nitrophenol or nitroarenes under ambient conditions is not actively considered [63–68]. Here, we demonstrate that the way to enhance the catalytic activity of aluminophosphates is through the substitution of Fe and/or Co in the structure of aluminophosphates. We used our synthesized transition metal (TM)-doped aluminophosphate (TM-APO) zeolite samples (both the 550 °C pyrolyzed samples and the 1000 °C calcined samples) as photocatalysts to investigate their effectiveness in reducing the hazardous 4-nitrophenol (NP) to the very useful 4-aminophenol (AP) through the use of NaBH$_4$. This reduction reaction was carried out in a photocatalytic reactor setup as discussed earlier (Figure S6). UV–Vis spectroscopy was used to evaluate the effectiveness of the catalysts quantitatively.

Figure 11 shows the UV–Vis absorbance spectra recorded after allowing the reduction of the NP-solution to occur for several time durations without using a catalyst or in presence of the pure aluminophosphate as catalyst. Note that, as stated in the experimental details, in all the cases, a fixed amount (50 mg) of the catalyst was used in the NP solution containing 180 mL of (0.0414 M) NP solution along with 20 mL of (1.5 M) NaBH$_4$. By the addition of NaBH$_4$ into the solution, the solution changes its color from faint yellow to straw yellow, which indicates the formation of 4-nitrophenolate ion. By adding an active catalyst, the solution becomes colorless in a few minutes of time duration, depending on the effectiveness of the catalyst. This color change indicates the conversation of NP to AP. The intensity of the UV–Vis spectra (Figure 11) quantitatively confirms the decrease in peak intensity of the peak at ~400 nm (corresponding to light absorption by the 4-nitrophenolate ion) and a simultaneous increase in intensity of the peak at ~292 nm (corresponding to light absorption by the 4-aminophenolate) without forming any by-products.

The rate of reaction (pseudo-first order), i.e., the rate constant (K_a) of the reaction was estimated by using the pseudo-first-order rate kinetic relation as follows:

$$-\ln\left(\frac{A_t}{A_0}\right) = K_a t \tag{1}$$

where, A_t and A_0 are the intensities of the absorption spectra at time 't' and '0' (initial value), respectively [69]. For evaluation of the rate of reaction, the concentration of 4-nitrophenol was calculated using the integrated intensity of the nitrophenolate peak in the UV-Vis spectra. The apparent rate constants (K_a) of the reactions were estimated using the pseudo-first-order rate kinetic relation and are given in Table 5. The value of K_a is considered from the slope after the initial 'induction time'. Clearly, for both the cases (without any catalyst or in presence of pure aluminophosphate as catalyst), we did not

observe any appreciable 4-nitrophenol reduction activity (Figure 11c). It is also known that, in the absence of a catalyst, $NaBH_4$ alone cannot reduce the NP molecules, but it helps in reducing NP to AP in presence of a catalyst [70] hence an active catalyst is necessary.

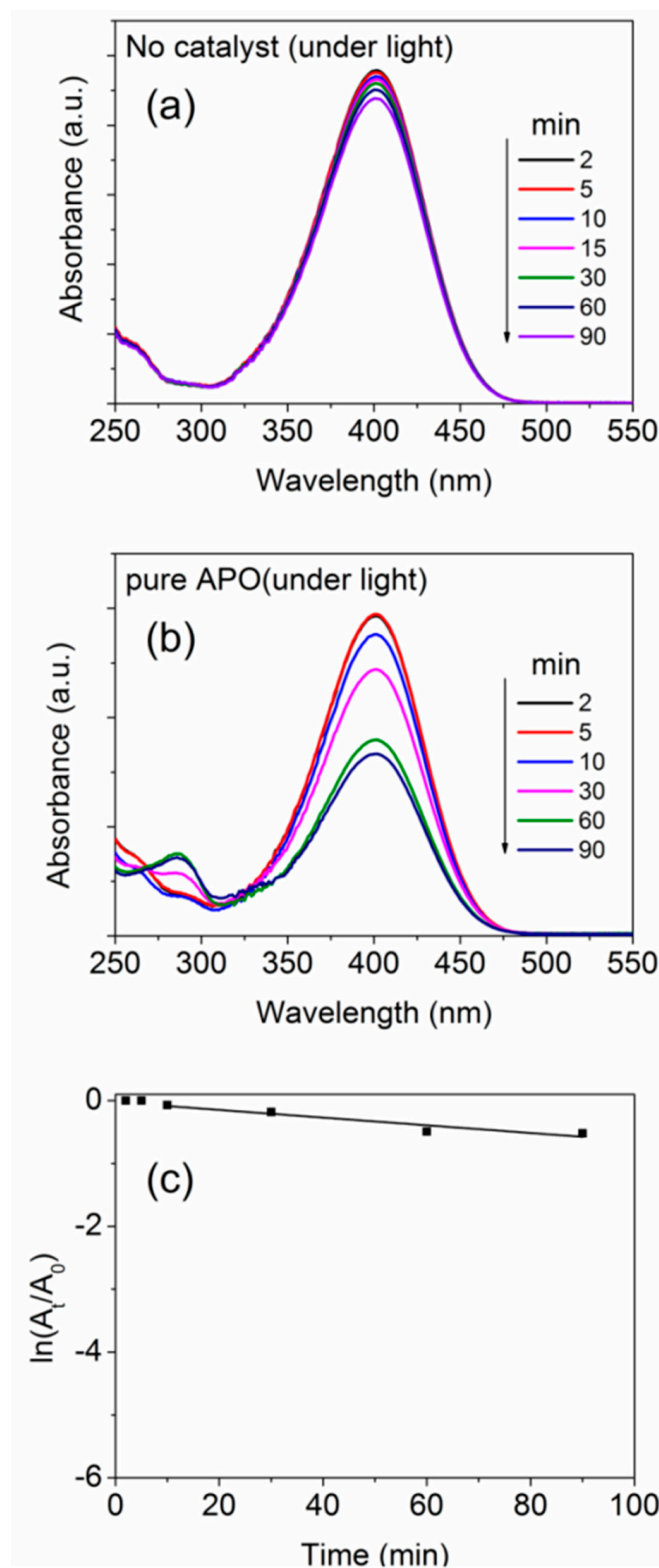**Figure 11.** UV-Vis absorbance spectra after different time durations (**a**) without catalyst and (**b**) with pure APO samples, undergoing NP reduction. (**c**) Plots showing the time-dependent change in absorption intensity for the NP reduction reaction.

Table 5. Induction time (I_t), rate of reduction after induction time (K_a), and % conversion (after 90 min) of 4-nitrophenol to 4-aminophenol using the synthesized aluminophosphates.

Sample	Dark			Light			Light + Pre-Stirring		
	I_t (min)	K_a (min^{-1})	% Conversion	I_t (min)	K_a (min^{-1})	% Conversion	I_t (min)	K_a (min^{-1})	% Conversion
CoAPO-550	5	−0.066	97	2	−0.126	100	-	-	-
FeAPO-550	15	−0.010	52	15	−0.010	49	-	-	-
CoFeAPO-550	15	−0.011	62	10	−0.053	99	-	-	-
CoAPO-1000	27	−0.028	84	9	−0.058 (−0.039)	94	-	−0.235 (−0.043)	100
FeAPO-1000	52	−0.034	71	33	−0.011	91	12	−0.074	100
CoFeAPO-1000	9	−0.004	42	10	−0.021	90	9	−0.061	100

In most of the earlier studies, metal nanoparticles have been used as catalysts for this 4-NP reduction reaction under ambient conditions, where it was known that the rate of reaction depends on the number of active sites and concentration of NaBH$_4$ [71]. However, the limitation associated with the metal catalysts are that they are either too expensive or degrade under ambient conditions, along with the cumbersome synthesis procedure often associated with them. In search of stable and economical catalysts with fast reaction kinetics and high turnover frequency, herein, we investigated the effectiveness of our TM-APO samples (both types: pyrolyzed in Ar and calcined in Air). The UV–Vis absorbance plots for NP-reduction by the (550 °C) pyrolyzed samples are shown in Figure 12. In comparison to the pure APO sample (Figure 11), these pyrolyzed samples show moderately higher catalytic activity (Figure 12, left panel, under dark condition), which is further enhanced in the presence of light (Figure 12, right panel). From the slope of the time dependent absorbance plots (Figure 12d,h), it is clear that the improvement in catalytic activity under light is negligible for the FeAPO-550 sample; however, for the CoFeAPO-550 sample, it is the highest. Furthermore, among all the pyrolyzed samples, the CoAPO-550 sample shows good catalytic activity, both in dark and under light. The origin of catalytic activity of our samples is related to both the microscopic and macroscopic structural aspects of the samples. The highest catalytic activity shown by the CoAPO-550 sample, even in dark conditions, can be understood by the charge state of Co, where, instead of only Co^{3+}, a significant amount of Co^{2+} is also present, as observed by XPS (Figure 7). This difference in charge state creates oxygen vacancies, especially in the CoAPO sample, and the vacancies possess negative electronic charge (electrons). These electrons help in originating the higher catalytic activity in CoAPO samples, even in the dark. As a relatively smaller number of Co^{2+} cations (in CoFeAPO-550 sample) or almost no Fe^{2+} cations are expected (in FeAPO-550 sample, Figure 6), in addition to the thicker carbon layer covered on these APO-based particles, these samples do not show good catalytic activity in dark condition.

Let us understand the origin of the observed photocatalytic activity of these pyrolyzed samples under light. It is clear from the analysis of the XRD, SEM, and TGA results that the pyrolyzed samples contain a lot of amorphous carbon and they appear black in color. Hence, the exposed surface for catalytic reaction for these samples is not the surface of the APO-based particles but the amorphous carbon covering, suggesting that the catalytic activity is mostly contributed by the amorphous carbon layer covering on the APO-based particles, in addition to its role in influencing the catalytic activity of the APO-based particles underneath. Furthermore, from the SEM/TEM and TGA results, we observed that the amount/thickness of the amorphous carbon covering is the highest for the FeAPO-550 sample, followed by CoFeAPO-550, and CoAPO-550. The pure APO-550 sample has the least amount of amorphous carbon covering. Correlating the amount of amorphous carbon with the catalytic activity shown by the samples (Figure 12d,h) in the dark and under the light, it can be rationalized that there is a remarkable contribution of light to instigate the catalytic activity of the samples. This aspect can be understood from the analysis of the UV–Vis DRS results, as discussed below.
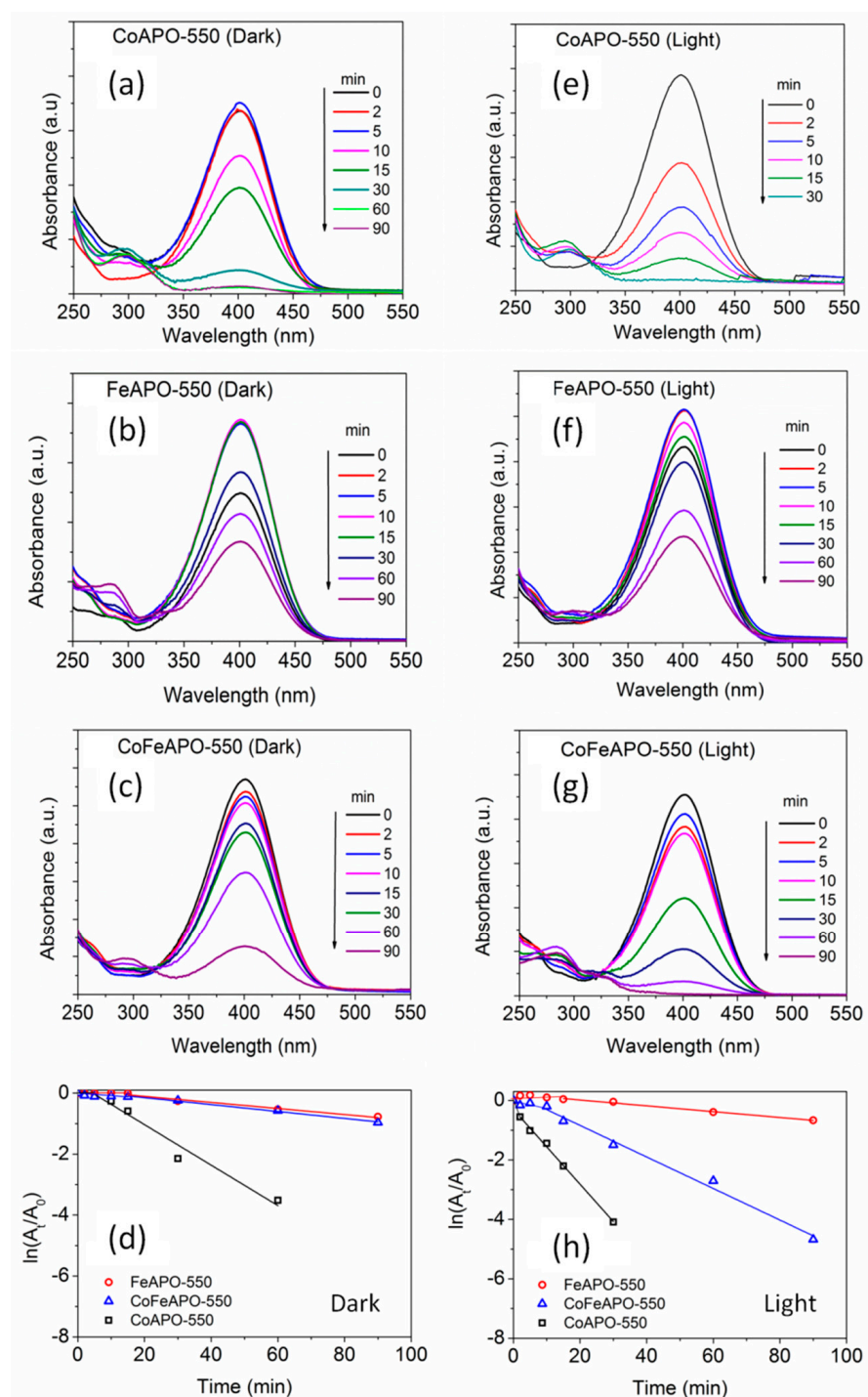
Figure 12. The UV-Vis absorbance spectra of the NP solution after certain interval of time, as indicated. The (550 °C) pyrolyzed samples were used as catalysts under dark and light conditions. Left panel (under dark): (**a**) CoAPO-550, (**b**) FeAPO-550, and (**c**) CoFeAPO-550 samples as catalysts for NP reduction; and right panel (under light): (**e**) CoAPO-550, (**f**) FeAPO-550, and (**g**) CoFeAPO-550 samples as catalysts for NP reduction. (**d,h**) The plots showing the time-dependent change in absorption intensity for the NP reduction reaction. The lines are to guide the eye.

As will be made clear from the mechanism of catalytic activity of our APO-based samples, the availability of electrons on the surface of the particles is important for facilitating the catalytic reduction of NP to AP. In this respect, the following factors decide the activity of the light in enabling a catalytic reaction: (1) the creation of electron–hole pairs

in the APO-based catalyst by the incident light, (2) the transition of these electrons to the conduction band of the APO-based material, and (3) the transport of these electrons onto the surface of the particles through the carbon coating. In the analysis of the UV–Vis DRS results (Figure 8a), we have observed that the pyrolyzed samples with the average energy gap (bandgap) of between 1.3 and 1.5 eV absorb the photons in the whole measured UV–Vis frequency region. This absorption behavior can be associated with occurring at the carbon covering only [30,32–34,42], and the core APO-based particles are partially shielded by the light absorption at this carbon covering. From the TGA results, we have observed that the weight loss associated with the burning of carbon occurs at ~500 °C for the FeAPO-550 and CoFeAPO-550 samples, whereas it occurs at ~600 °C for the CoAPO-550 sample. Hence, the carbon covering on the CoAPO-550 sample is more graphitic (and thinner) in nature. As graphitic carbon is more conducting than the amorphous carbon and thickness of the graphitic layer is lower (in the CoAPO sample than that of the other samples), the photo-excited electrons are easily transported to the surface of the CoAPO samples. Hence, under light, the CoAPO-550 sample shows the highest activity followed by the CoFeAPO-550 sample. Based on the BET and UV–Vis-DRS results, the CoFeAPO-550 sample should have shown the highest activity. This discrepancy could arise due to a higher number of defects or better crystallinity of the CoAPO samples, as discussed later.

The reduction of NP to AP using the graphene/graphite-type carbon as a catalyst has been studied earlier and are available in the literature [72,73]. As our samples contain APO-based nanoparticles with a carbon covering, the carbon covering can directly contribute towards 4-NP reduction. However, as the amorphous carbon has lower conductivity than graphene- or graphite-type carbon, they are not efficient for hydride formation. The hydride formation mechanism will be discussed later. Hence, among all our pyrolyzed samples, as the CoAPO-550 sample has better graphitized carbon, this sample shows better catalytic activity. In essence, the presence of better graphitic carbon helps both in conduction and hydride formation. This carbon covering also protects the underlying nanoparticles from degradation [35–37].

Furthermore, since the surface area of the carbon-coated samples (prepared at 550 °C) is higher than calcined samples, they should show better catalytic activity. Based on the UV–Vis DRS results, it can be rationalized that apart from surface area, other factors like bandgap and crystallinity also play a role in catalytic NP reduction. The carbonaceous layer in pyrolyzed samples imparts quite a high surface area to them, which would allow good adsorption and catalytic activity. But to identify the mechanism and role of aluminophosphate structure in 4-nitrophenol reduction, the study of the samples annealed to 1000 °C (devoid of carbon layer) becomes imperative. These aspects had not yet been studied and thus a comprehensive study in this regard was required.

Now, let us consider the catalytic activities of the 1000 °C calcined samples. The UV–Vis absorbance plots for the corresponding NP reductions are shown in Figure 13. The 1000 °C calcined samples show the activities and trends comparable to the pyrolyzed samples (Figure 14). We studied the detailed reaction kinetics for these samples calcined at 1000 °C (Figures 13 and 14), using three conditions, viz. dark, under intense UV–Vis light, and with pre-stirring and intense UV-Vis light. In the first two sets of experiments in the dark and under the light, the measurements started as soon as catalyst was added. In the third set, an initial 30 min pre-stirring of the solution (under dark) with catalyst (without $NaBH_4$) was allowed, followed by adding the $NaBH_4$, switching on Xenon lamp, and starting the measurements. Among all the samples, the Co-based samples show the highest catalytic activities. Figure 14 depicts the time-dependent rate curves derived from the UV–Vis absorbance plots (Figure 13). As mentioned earlier, the apparent rate constant (K_a) is considered from the slope of the linear region after the initial induction time. The values of the rate constants and induction times are given in Table 5. The catalytic activities of the samples are higher in the presence of light compared to the dark, clearly indicating the involvement of the photo-generated electrons and holes in enhancing the catalytic activity. Further, when pre-stirring (without $NaBH_4$) is employed, there is a drastic reduction

in the induction times for the samples, suggesting that the induction time is related to initial adsorption of the reactant species. When pre-stirring along with light is involved, CoAPO-1000 shows a near complete reduction within 30 min of the reaction time. The near stagnancy of data points beyond 30 min (Figure 14b,c) is due to inadequacy in reliable calculation of low intensity from UV–Vis absorbance plots (Figure 13c). Furthermore, we can clearly observe that the induction times of the calcined samples, especially the Fe-based samples, are significantly higher than pyrolyzed ones. The origin of the induction times and their detailed mechanism are discussed in next section.
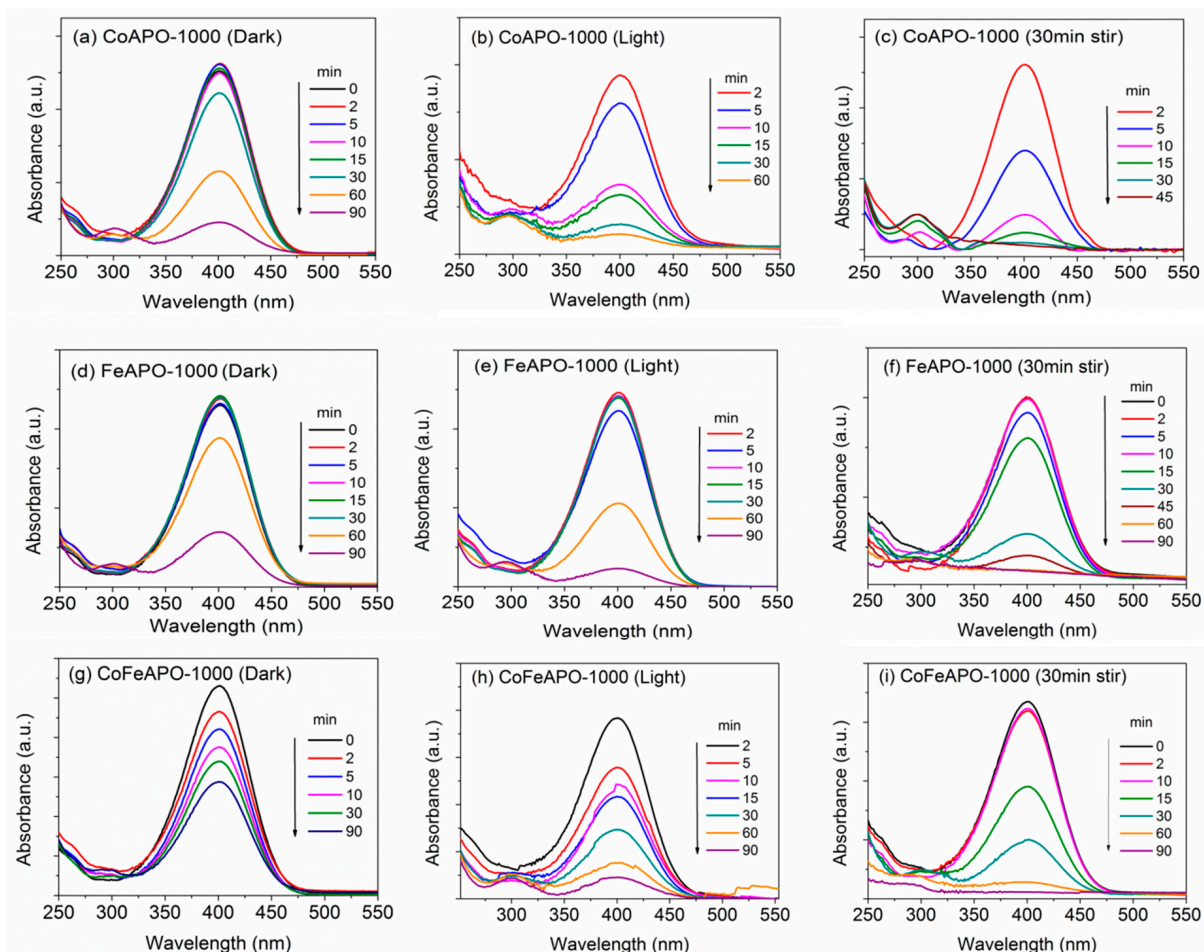

Figure 13. UV-Vis absorbance plots for annealed samples (1000 °C) undergoing NP reduction in the dark (left panel): (**a**) CoAPO-1000, (**d**) FeAPO-1000, (**g**) CoFeAPO-1000; under the light (middle panel): (**b**) CoAPO-1000, (**e**) FeAPO-1000, (**h**) CoFeAPO-1000; and under the light with pre-stirring (right panel): (**c**) CoAPO-1000, (**f**) FeAPO-1000, (**i**) CoFeAPO-1000.

The UV–Vis DRS plots (Figure 8) show that the CoFeAPO-1000 can absorb in both UV and visible ranges. Based on these characterization results, we expected that among the samples prepared at 1000 °C, CoFeAPO-1000 should show the highest catalytic activity. Surprisingly, this is not the case. In fact, its catalytic activity is the lowest. The residual carbon content (Figure 5, Table S2) is the lowest, which leads to a low induction time. The high induction time of FeAPO-1000 could be attributed to the residual carbon on the surface of the nanoparticles, because carbon has a hydrophobic nature. But the low catalytic activities of FeAPO-1000 and CoFeAPO-1000 can be related to their higher bandgap and lower crystallinity. These aspects are discussed further in the mechanism provided in the section below.
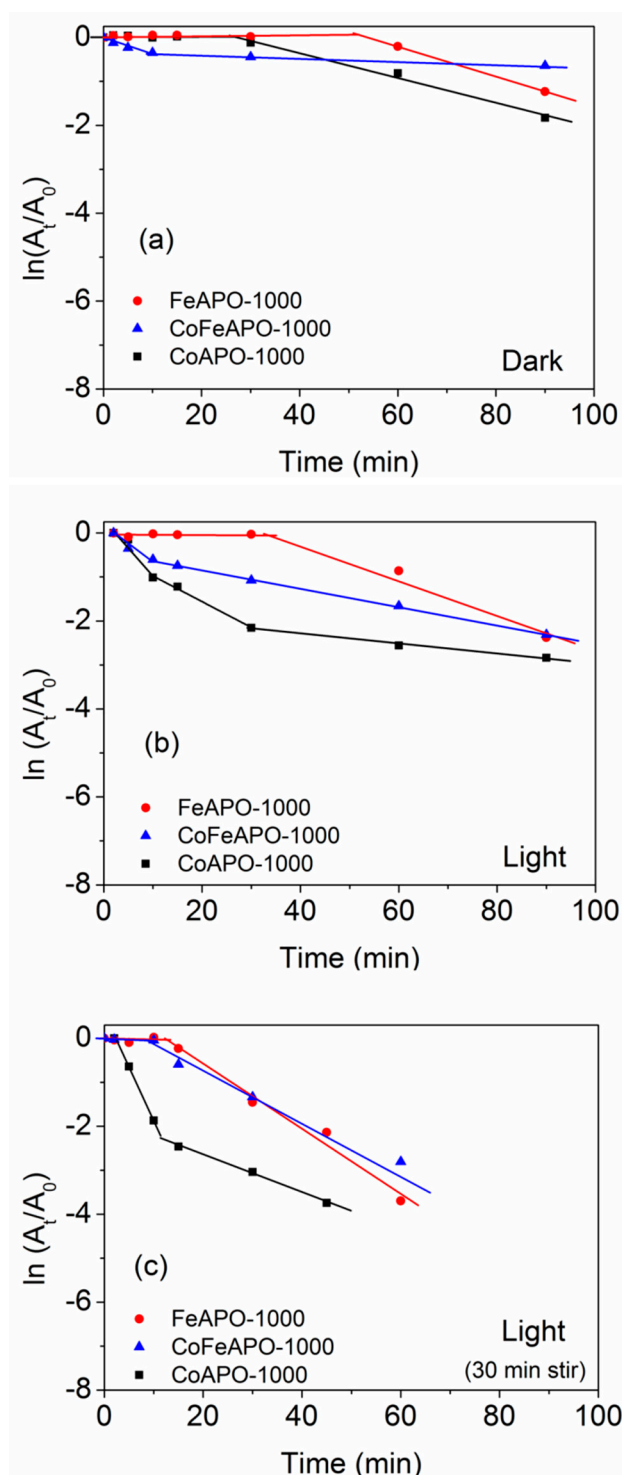
Figure 14. Time-dependent absorption plots of the NP reduction reaction for samples annealed at 1000 °C in the (**a**) dark, (**b**) light, and (**c**) light with pre-stirring. The lines are a guide to the eye.

Induction Time and Mechanism of Catalytic Reduction of 4-NP by the TM-APO Samples

In most of the cases, the catalytic reaction does not start instantly as soon as the catalyst is added to the reactants due to several reasons such as the hydrophobic nature of the surface and their surface energy/chemical potential; rather, it takes some time, varying from a few seconds to a few tens of minutes, depending on the catalysts. This time is known as the induction time. In all our samples, we observed an initial 'induction time', which was more dominant in Fe-based samples that showed lower activity. The induction time phenomenon

has been observed by other researchers and ascribed to surface restructuring of catalysts before the onset of a reaction [11,71]. Menumerov et al. observed that this induction time was higher in solutions containing dissolved oxygen [74] and essentially negligible in catalysts showing high catalytic activity, and in the absence of dissolved oxygen. However, any other justification supporting their claim is not satisfactorily provided in those references. In our case, we did not remove the dissolved oxygen, i.e., all the conditions were the same for all our experiments. Therefore, the observation of variable induction times cannot be strongly ascribed to the issue of dissolved oxygen or the surface restructuring.

Let us consider the induction time observed in our pyrolyzed samples first. In all the samples, the APO-based nanoparticles were covered by a carbonaceous layer. If we analyze the TGA data carefully (Figure 5, Table S2), we observe that FeAPO-550 has a higher amount of carbon followed by CoFeAPO-550. Both these samples show high induction times. The carbon layer is quite amorphous as visualized from the XRD data. Although this layer imparts a high surface area to the samples, apparently, the amorphousness of the carbon layer does not allow for the fast absorption of the reactants, which leads to a high induction time. In the presence of light, this induction time does not change appreciably and therefore the induction times in these samples are controlled by the nature of the amorphous carbon-type surfaces. The enhancement of catalytic activity in the presence of light indicates that the electronic properties of the doped-APO structure play the dominant role, since the carbonaceous layer will essentially contribute similarly in all pyrolyzed samples. In other words, it suggests that the efficiency of the carbon layer is less than that of the doped-APO towards 4-nitrophenol reduction.

The residual carbon in calcined samples can impart a thin graphenic (hydrophobic) layer covering and contribute towards increasing induction time. Hence, the variation in induction times for calcined samples could have originated from the amount of % residual carbon (Table S2, ESI). But comparing the FeAPO-550 and FeAPO-1000 samples (Figure 5), where the calcined sample shows very high induction time compared to the other counterparts, having only about ~1.3% of residual carbon left from the initial 21%, we can understand that the surface (amorphous) carbon layer is not the sole contributor here. Rather, it may be possible that the catalyst surface, which has high number of O-atoms or surface defects associated with the APO structure, contributes in enhancing the induction times.

In the initial catalytic reaction process, the borohydride ion (BH_4^-) and 4-nitrophenolate adsorb onto the catalyst surface and then undergo hydride transfer to yield 4-aminophenol. It can be understood that electron transfer would be vital to this process, but it has not been clearly stated in the literature. There may be several pathways involved in the catalytic reduction process such as water reduction and hydride transfer resulting in numerous intermediates. Such information requires highly sophisticated in situ spectroscopic analysis. We do have many reports of metal nanoparticles as good catalysts rather than for oxides for this reaction. It is expected that the surfaces with a high amount of oxygen groups (rather than the amorphous carbon structure) will perform poorly towards the initial adsorption of the reactants. This explains the relatively high induction times in all the Fe-based samples (as well as the calcined samples). The improvement in catalytic activity in the presence of light compared to the dark confirms the role of electrons in this process, similar to the results of the previous reports [75–78]. Additionally, from the XPS analysis, we know that Co exists in both the 2+ and 3+ states. Since Co^{2+} cations replace Al^{3+}, some extra electrons would have come into the APO structure and lead to oxygen vacancies. These would, in turn, act as active sites for adsorption of the negatively charged reactants. Further, an electronically conductive surface would allow for the easy flow of electrons and assist in hydride transfer. It may be observed that under intense UV–Vis light, electrons and holes are generated in the case of the doped samples due to their semiconducting nature. The generated photoelectrons should assist in speeding up the hydride transfer affecting faster rate kinetics [79]. According to the literature, the holes can also lead to the formation of •OH radicals (water reduction) which can degrade the 4-nitrophenol [80–84]. The recent

literature confirms that the hydrogen source during 4-nitrophenol reduction can be both borohydride and protic solvents like water [85,86], albeit via different reaction pathways.

　　In all the samples, we see enhanced catalytic activity in the presence of light (Figures 13 and 14). In the case of CoAPO-1000, which shows the best catalytic activity, the defect density (inferred from the Urbach energy, Figure S5, ESI) is the lowest. Low defect density allows the holes and electrons to reside near the band edge, which can facilitate their easy transfer to the reactants (on the surface of the catalysts). The third set of experiments, where we allowed pre-stirring of the catalyst along with 4-nitrophenol (without NaBH$_4$ and before shining the light), confirms that the induction time for our samples is dependent on the initial adsorption of both the reactants, rather than the hypothetical removal of boro-hydride by dissolved oxygen as reported, e.g., in ref. [74]. Another group also considered this induction time to be due to the removal of surface oxides by NaBH$_4$ [87]. Since we did not add NaBH$_4$ during the pre-stirring stage but observed a drastic reduction in induction time, the induction time is related to the slower rate of adsorption. Hence, an initial dynamic restructuring of the catalyst surface, as suggested by Wunder et al. [11,71,88] and others [89], may be discarded in the case of our samples. The pre-stirring of the solution along with the catalyst provides sufficient time for the adsorption of the hydride and the 4-nitrophenolate onto the active sites, thereby reducing the induction time. Thus, our work helps in resolving the debate surrounding the origin of induction time in 4-nitrophenol reduction and opens the path for utilization of aluminophosphates for this industrially important catalytic reaction. Based on the observations, we have proposed a mechanism for the 4-nitrophenol reduction process (Figures 15 and 16). NaBH$_4$ ionizes in the solution to give borohydride ions, which give electrons to the catalyst surface, simultaneously forming the catalyst–H bonds (Figure 15a). The adsorbed hydrogen can combine with the OH$^-$ ion to form water (Equation (2)) or combine to form H$_2$ [85].
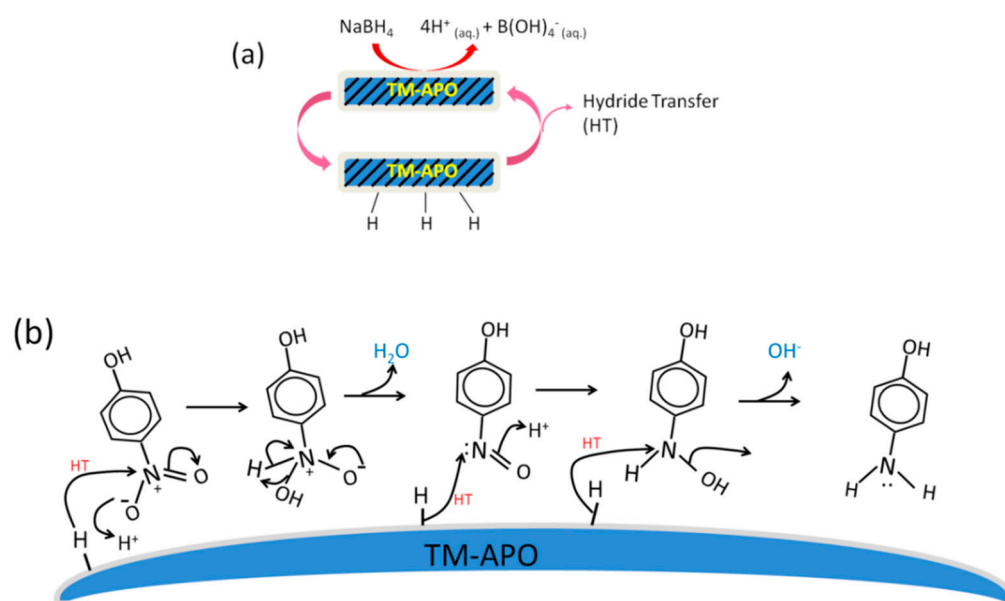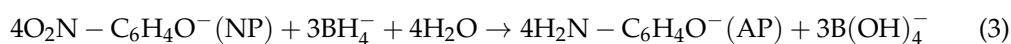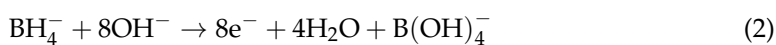
$$BH_4^- + 8OH^- \rightarrow 8e^- + 4H_2O + B(OH)_4^- \tag{2}$$

$$4O_2N-C_6H_4O^-(NP) + 3BH_4^- + 4H_2O \rightarrow 4H_2N-C_6H_4O^-(AP) + 3B(OH)_4^- \tag{3}$$

Figure 15. Schematics depicting (**a**) the adsorption of hydrogen onto the surface of samples, and (**b**) the general mechanism of 4-nitrophenol reduction using our samples via hydride transfer.
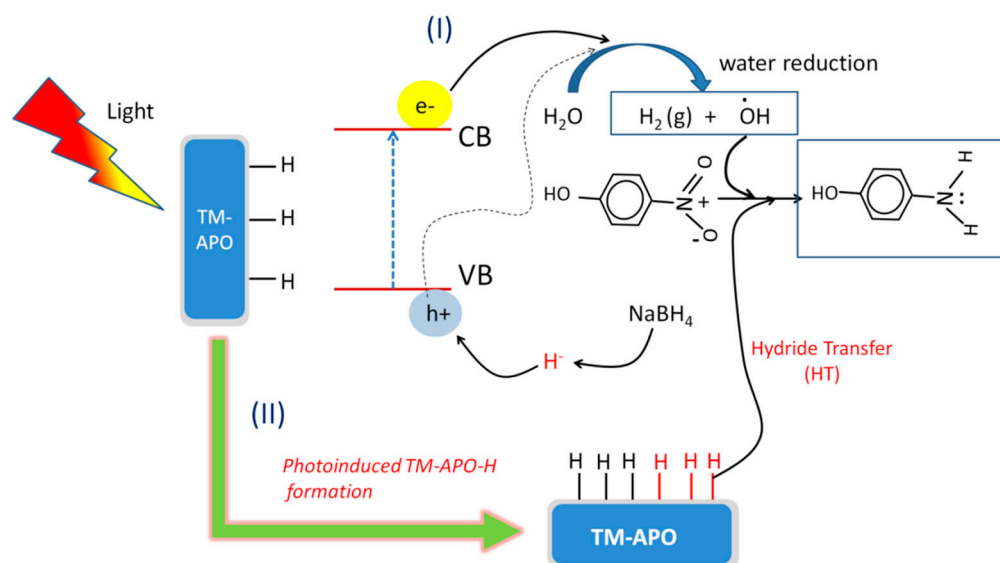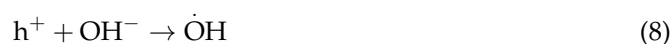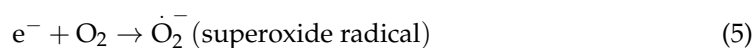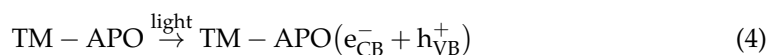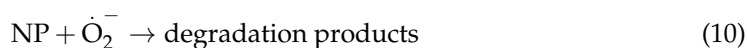
Figure 16. Schematic depicting the mechanism of 4-nitrophenol reduction in presence of light using our (TM-APO) samples.

The electrons are then transferred to the reaction center of the nitro groups from the catalyst surface, and the protons are obtained from water [85] (Equation (3)), although the most commonly reported reduction route is the hydride (H^-) transfer (Figure 15b). The reaction is adequately fast in dark conditions and involves three hydride addition steps as shown in Figure 15b.

In general, during the first hydride transfer, the nitro group simultaneously interacts with H^+ from the solution and forms an –OH bond, followed by the elimination of water molecules. The electron-rich intermediate nitroso compound then attracts another hydride transfer and the concerted addition of H^+ available from the solution. The third hydride transfer facilitates the loss of the OH^- ion and conversion to an amino group. After each hydride transfer, the active site is regenerated, and further adsorption of the incoming hydride occurs.

In the presence of light, additional pathways can be utilized during NP reduction. Alongside the conventional hydride transfer route (as discussed above and shown in Figure 15), water reduction can also assist in NP reduction. Further, hydride transfer can be significantly enhanced by photo-induced enhanced adsorption of hydride on the catalyst surface. As shown in Figure 16, the incident light on our semi-conducting samples can generate additional electrons and holes, which can also take part in the reduction process. The electron- and hole-mediated photocatalytic reduction reaction can be understood from the following reactions (Equations (4)–(11)).

$$\text{TM} - \text{APO} \xrightarrow{\text{light}} \text{TM} - \text{APO}\left(e^-_{\text{CB}} + h^+_{\text{VB}}\right) \tag{4}$$

$$e^- + O_2 \rightarrow \dot{O}_2^- \text{ (superoxide radical)} \tag{5}$$

$$\dot{O}_2^- + 2H^+ + 2e^- \rightarrow OH^- + \dot{O}H \tag{6}$$

$$h^+ + H_2O \rightarrow H^+ + \dot{O}H \tag{7}$$

$$h^+ + OH^- \rightarrow \dot{O}H \tag{8}$$

$$NP + \dot{O}H \rightarrow \text{degradation products} \tag{9}$$

$$NP + \dot{O}_2^{-} \rightarrow \text{degradation products} \tag{10}$$

$$2H^+ + 2e^- \rightarrow H_2 \tag{11}$$

The holes can interact with the incoming hydride, facilitating more adsorption, i.e., the formation of a higher number of catalyst–H bonds. The quenching of the photogenerated holes by the highly reactive hydrides delays the electron–hole recombination [75]. Alternatively, the holes can also reduce water and generate •OH radicals. In conclusion, there can three synergistic pathways involved in the 4-nitrophenol reduction in presence of light as follows [75]: (a) hydride transfer from catalyst surface, (b) photo-generated hydride transfer from the catalyst surface, and (c) hydrogen transfer from the photo-reduced water. Thus, it can be understood that presence of light enhances the 4-nitrophenol reduction using our synthesized catalysts.

4. Experimental Details

In this work, Fe- and/or Co-incorporated aluminophosphate samples were synthesized by the hydrothermal synthesis method using the procedure given schematically in Figure 17. In brief, phosphoric acid (1.4 mL) was initially diluted with 11.7 mL of deionized water (DI). Then, 4.08 g (40 mmol) of aluminum isopropoxide ($Al(O-CH(CH_3)_2)_3$) was added, with vigorous stirring. Following that, 0.37 g (1.5 mmol) of cobaltous acetate [$Co(acac)_2 \cdot H_2O$] was dissolved in 5 mL of DI water and the solution was added to the above mixture. The mixture was then stirred for 1 h at 70 °C, after which tetramethyl ammonium hydroxide (TMAOH, 7.3 mL) was added dropwise to form a slurry. The slurry was stirred for 3 h (at RT), followed by the addition of cetyl tetra-ammonium bromide (CTAB, 3.64 g). An additional 20 mL of DI water was then added. The mixture was stirred for another 12 h. The pH of the dispersion was maintained at ten (10) by the addition of liquor ammonia. The final mixture was transferred to a Teflon-lined autoclave and kept at 160 °C inside a muffle furnace for 72 h. The resultant solid was filtered through a Büchner funnel, repeatedly washed with distilled water, and dried at 70 °C in a hot-air oven for 12 h.
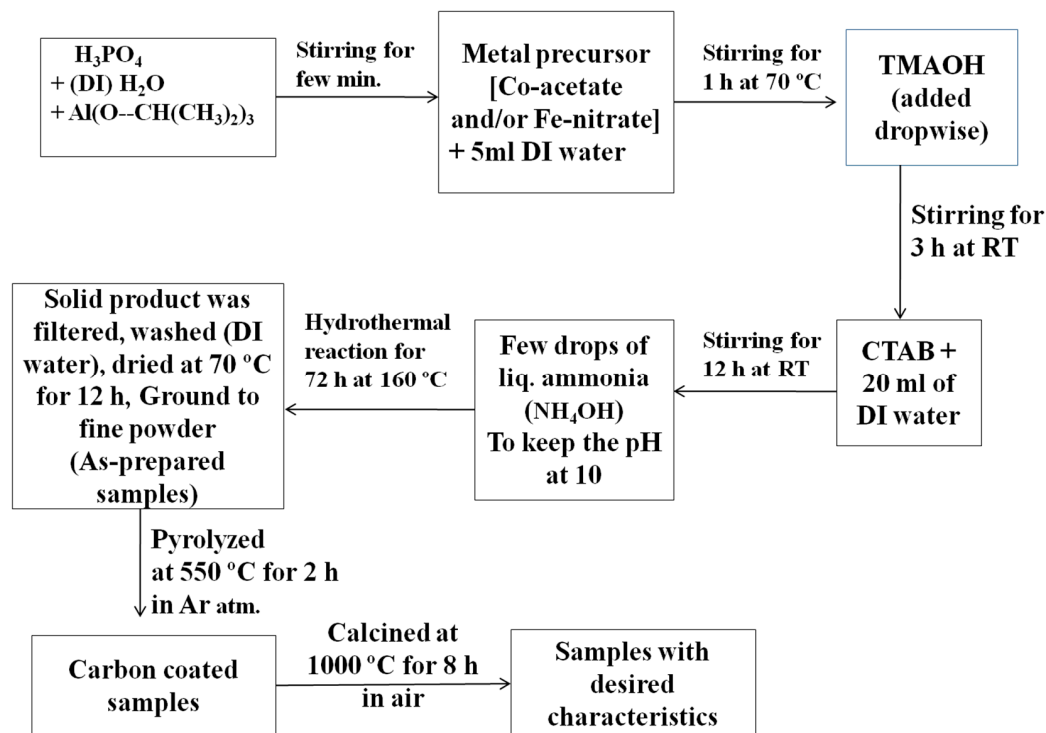

Figure 17. The procedure used for the hydrothermal synthesis of transition metal-doped aluminophosphate samples, followed by a few steps of thermal treatment.

Using the same procedure, we prepared Fe-doped aluminophosphates, where the experiments were performed using iron nitrate (0.606 g, 1.5 mmol) instead of cobaltous acetate. Furthermore, using an equimolar composition of both cobaltous acetate (0.186 g, 0.75 mmol) and iron nitrate (0.303 g, 0.75 mmol), another sample was also prepared. The above three as-prepared samples were labelled as CoAPO-asp, FeAPO-asp, and CoFeAPO-asp, respectively (the doped transition metals are given at the beginning of the code). The sample compositions were $Co_{0.048}Al_{0.952}PO_4$ (CoAPO), $Fe_{0.07}Al_{0.93}PO_4$ (FeAPO), and $Co_{0.024}Fe_{0.034}Al_{0.942}PO_4$ (CoFeAPO). As will be clear later, there exists a carbonaceous layer (associated with the precursors) on the surface of the particles of the as-prepared samples. To control this layer and to enhance the activity of the powder particles, the powders were initially pyrolyzed at 550 °C in argon atmosphere and then calcined at 1000 °C in air. For the pyrolysis of the dried powders, the respective as-prepared samples were placed in a closed-end quartz tube of 50 cm length and 1 cm diameter, which was attached with a rubber bladder (filled with argon gas) at the open end [25–34]. The sample was then heated to 550 °C at a rate of 20 °C min^{-1} and kept for 2 h to allow for the pyrolysis reaction to occur, before decreasing the temperature to RT. The obtained black-colored powders were labelled as CoAPO-550, FeAPO-550, and CoFeAPO-550. Part of these pyrolyzed products was placed separately in alumina crucibles and then annealed in air for 8 h in a muffle furnace at 1000 °C. The products were labelled as CoAPO-1000, FeAPO-1000, and CoFeAPO-1000. For comparison, pure APO samples (without any doping) were also synthesized using the same procedure.

All the as-synthesized and calcined samples were characterized using analytical and spectroscopic techniques. The powder X-ray diffraction (XRD) patterns were recorded on a 'PANalytical' X-ray diffractometer. Rietveld refinement was performed to understand the doping of the transition metals in the APO lattice. Scanning electron micrographs were imaged using an 'Ultra 55' electron microscope. Transmission electron micrographs (TEM) were imaged on a 'JEOL' FETEM (300 kV). Furthermore, ^{57}Fe Mössbauer spectra were recorded at room temperature using (SEE Co, USA) a spectrometer in transmission geometry with a ^{57}Co source (Rh matrix). The data were fit using NORMOS 2 software. Thermogravimetry analysis (TGA) measurements were performed in a 'TA Q50' system in a nitrogen atmosphere (40 mL min^{-1}) at a heating rate of 10 °C min^{-1}. The net surface area was determined through Brunauer–Emmett–Teller (BET) isotherms, while the pore size in the samples was determined by the Horvath–Kawazoe (HK) method. Ultraviolet–Visible Diffuse Reflectance Spectra (UV-DRS) were recorded on a Perkin Elmer Lambda 750 spectrophotometer in the wavelength range of 250–800 nm, with barium sulfate as the standard. For calculation of bandgap, the reflectance (R) data recorded directly from the instrument were converted into Kubelka–Munk function F(R) using the Kubelka–Munk equation as follows [30–32]:

$$F(R) = \frac{(1-R)^2}{2R} \tag{12}$$

where, F(R) is the Kubelka–Munk function and R is the reflectance.

The catalytic behavior of our samples was examined through the 4-nitrophenol reduction reaction. For a typical catalysis experiment, 180 mL (0.0414 M) of NP solution and 20 mL (1.5 M) of $NaBH_4$, along with 50 mg of the catalyst (dispersed in the stock solution) was taken in a photo-reactor (Lelesil Innovative Systems). In this setup, a Xenon UV lamp was coaxially placed inside the U-tube (Figure S6, ESI) after the reactants for the photo-catalysis reaction were added. The initial experiments were performed in the dark. In subsequent experiments, the solution was then irradiated with UV–Vis light with constant and continuous stirring of the solution (using a magnetic stirrer setup). After different durations of the catalytic reaction, viz. 0, 2, 5, 10, 15, 30, 60, and 90 min, about 5 mL of the solution was taken out each time from the reactor (stock solution), and the UV–Vis spectra were recorded using the UV–Vis spectrometer. A visual change in color of the solution, from yellow to colorless, after some interval of time also indicated the occurrence of the catalytic reaction.

5. Conclusions

Co- and Fe-doped aluminophosphate (APO) zeolites are synthesized by hydrothermal method. The as-prepared samples are pyrolyzed at 550 °C in Ar atmosphere, followed by calcination in the air at 1000 °C. The pyrolyzed co-doped sample has the highest surface area while the calcined samples have considerably low surface area. The calcined samples contain some residual carbon. All these samples are electrically semiconducting in nature. The bandgap of calcined FeAPO- and CoFeAPO-based samples are higher than the calcined CoAPO sample. The XPS and Mossbauer results confirm that a mixed valence state for the transition metals exists in the doped APO samples. The catalytic activity of the samples was studied using 4-nitrophenol reduction as model reaction. Interestingly, we observed that Co-based samples performed the best, although they have a lower surface area. We also observed a significant enhancement of the catalytic activity in the presence of light, which validates the roles of the photo-generated electrons and holes in the catalytic process. In all the cases, induction time was observed, especially in the less active catalysts, which can be ascribed to the initial adsorption of the reactants onto the catalyst surface. This phenomenon was considerably reduced by pre-stirring the solution with the catalyst (without $NaBH_4$) prior to starting the measurements. Our work helps in improving the current understanding regarding the mechanism of 4-nitrophenol reduction and the induction time, and their correlation with the surface area, electronic conductivity, bandgap, and crystallinity of samples, as they play important controlling roles.

Supplementary Materials: The following supporting information can be downloaded at: https://www.mdpi.com/article/10.3390/catal14070408/s1, Figure S1: The optical photographs of the APO and TM-doped APO-based powder samples, as indicated; Figure S2: The XRD patterns and the least-squares fitting through the Rietveld refinement for our calcined samples as indicated; Figure S3: Left panel: HRTEM of the (a) CoAPO-550, (c) FeAPO-550, and (e) CoFeAPO-550 samples pyrolyzed at 550°C. Right panel: HRTEM of the (b) CoAPO-1000, (d) FeAPO-1000, and (f) CoFeAPO-1000 samples calcined at 1000 °C; Figure S4: The XPS spectra of the FeAPO-1000 and CoFeAPO-1000 samples. The energy edge used is also indicated; Figure S5: Urbach energy plots for the samples calcined at 550 and 1000 °C; Figure S6: The reactor used for the photocatalytic studies. A Xe lamp was used, which is not switched on here; Figure S7: The time-dependent conversion depicted by color change in the collected aliquots during 4-nitrophenol reduction. The numbers written on the test tubes are the time duration in minutes for which the reduction reaction was studied; Figure S8: (a) Comparison of XRD patterns for the fresh CoAPO-1000 and recovered samples post-photocatalysis experiment. The (b) Co 2p, (c) P 2p, and (d) Al 2p XPS spectra for the recovered CoAPO-1000 sample; Table S1: The structural parameters obtained from the Rietveld refinement of the XRD patterns; Table S2: TGA weight loss %; **1**. Calculation of Urbach energy from UV–Vis DRS; **2**. The BET Method was used for the evaluation of the surface parameters from the adsorption–desorption isotherm.

Author Contributions: Conceptualization, R.K. and B.S.; methodology, R.K. and B.M.S.; software, B.S. and A.A.V.; validation, R.K. and B.S.; formal analysis, R.K., B.M.S., A.A.V. and B.S.; investigation, R.K., B.M.S., A.A.V. and B.S.; resources, F.Y. and B.S.; data curation, R.K., B.M.S. and S.K.; writing—original draft preparation, B.M.S., R.K., A.A.V. and B.S.; writing—review and editing, F.Y. and B.S.; visualization, R.K. and B.S.; supervision, B.S.; project administration, B.S.; funding acquisition, F.Y. and B.S. All authors have read and agreed to the published version of the manuscript.

Data Availability Statement: Data will be made available on request.

Conflicts of Interest: There are no conflicts of interest to declare.

References

1. Dapurkar, S.E.; Badamali, S.K.; Sakthivel, A.; Selvam, P. Isomorphous Substitution of Trivalent Iron in Mesoporous MCM-48 Silicate Molecular Sieves: Synthesis, Characterization and Catalytic Properties. *Bull. Catal. Soc. India* **2005**, *4*, 63–67.
2. Corma, A. From Microporous to Mesoporous Molecular Sieve Materials and Their Use in Catalysis. *Chem. Rev.* **1997**, *97*, 2373–2420. [CrossRef] [PubMed]
3. Sakthivel, A.; Selvam, P. Mesoporous (Cr)MCM-41: A Mild and Efficient Heterogeneous Catalyst for Selective Oxidation of Cyclohexane. *J. Catal.* **2002**, *211*, 134–143. [CrossRef]
4. Barton, T.J.; Bull, L.M.; Klemperer, W.G.; Loy, D.A.; McEnaney, B.; Misono, M.; Monson, P.A.; Pez, G.; Scherer, G.W.; Vartuli, J.C.; et al. Tailored Porous Materials. *Chem. Mater.* **1999**, *11*, 2633–2656. [CrossRef]
5. Cheetham, A.K.; Férey, G.; Loiseau, T. Open-Framework Inorganic Materials. *Angew. Chem. Int. Ed.* **1999**, *38*, 3268–3292. [CrossRef]
6. Rajić, N. Open-Framework Aluminophosphates: Synthesis, Characterization and Transition Metal Modifications. *J. Serbian Chem. Soc.* **2005**, *70*, 371–391. [CrossRef]
7. Cardile, C.M.; Tapp, N.J.; Milestone, N.B. Synthesis and Characterization of an Iron-Substituted Aluminophosphate Molecular Sieve. *Zeolites* **1990**, *10*, 90–94. [CrossRef]
8. Shiralkar, V.P.; Saldarriaga, C.H.; Perez, J.O.; Clearfield, A.; Chen, M.; Anthony, R.G.; Donohue, J.A. Synthesis and Characterization of CoAPO-5, a Cobalt-Containing $AlPO_4$-5. *Zeolites* **1989**, *9*, 474–482. [CrossRef]
9. Wang, L.; Tian, B.; Fan, J.; Liu, X.; Yang, H.; Yu, C.; Tu, B.; Zhao, D. Block Copolymer Templating Syntheses of Ordered Large-Pore Stable Mesoporous Aluminophosphates and Fe-Aluminophosphate Based on an "Acid–Base Pair" Route. *Microporous Mesoporous Mater.* **2004**, *67*, 123–133. [CrossRef]
10. Kraushaar-Czarnetzki, B.; Hoogervorst, W.G.M.; Andréa, R.R.; Emeis, C.A.; Stork, W.H.J. Characterisation of CoII and CoIII in CoAPO Molecular Sieves. *J. Chem. Soc. Faraday Trans.* **1991**, *87*, 891–895. [CrossRef]
11. Gu, S.; Wunder, S.; Lu, Y.; Ballauff, M.; Fenger, R.; Rademann, K.; Jaquet, B.; Zaccone, A. Kinetic Analysis of the Catalytic Reduction of 4-Nitrophenol by Metallic Nanoparticles. *J. Phys. Chem. C* **2014**, *118*, 18618–18625. [CrossRef]
12. Sharma, S.; Khare, N. Hierarchical Bi_2S_3 Nanoflowers: A Novel Photocatalyst for Enhanced Photocatalytic Degradation of Binary Mixture of Rhodamine B and Methylene Blue Dyes and Degradation of Mixture of p-Nitrophenol and p-Chlorophenol. *Adv. Powder Technol.* **2018**, *29*, 3336–3347. [CrossRef]
13. Sharma, M.; Hazra, S.; Basu, S. Synthesis of Heterogeneous Ag-Cu Bimetallic Monolith with Different Mass Ratios and Their Performances for Catalysis and Antibacterial Activity. *Adv. Powder Technol.* **2017**, *28*, 3085–3094. [CrossRef]
14. Anantharamaiah, P.N.; Chandra, N.S.; Shashanka, H.M.; Kumar, R.; Sahoo, B. Magnetic and Catalytic Properties of Cu-Substituted $SrFe_{12}O_{19}$ Synthesized by Tartrate-Gel Method. *Adv. Powder Technol.* **2020**, *31*, 2385–2393. [CrossRef]
15. Nagamine, S.; Inohara, K. Photocatalytic Microreactor Using Anodized TiO_2 Nanotube Array. *Adv. Powder Technol.* **2018**, *29*, 3100–3106. [CrossRef]
16. Liu, J.; Wu, Q.; Huang, F.; Zhang, H.; Xu, S.; Huang, W.; Li, Z. Facile Preparation of a Variety of Bimetallic Dendrites with High Catalytic Activity by Two Simultaneous Replacement Reactions. *RSC Adv* **2013**, *3*, 14312–14321. [CrossRef]
17. Gong, C.; Zhou, Z.; Zhou, H.; Liu, R. Vacuum-Assisted Synthesis of Tiny Au Nanoparticles Entrapped into Mesoporous Carbon Matrix with Superior Catalytic Activity for 4-Nitrophenol Reduction. *Adv. Powder Technol.* **2019**, *30*, 649–655. [CrossRef]
18. Tian, Y.; Cao, Y.Y.; Pang, F.; Chen, G.Q.; Zhang, X. Ag Nanoparticles Supported on N-Doped Graphene Hybrids for Catalytic Reduction of 4-Nitrophenol. *RSC Adv.* **2014**, *4*, 43204–43211. [CrossRef]
19. Kumar Barman, B.; Kar Nanda, K. Uninterrupted Galvanic Reaction for Scalable and Rapid Synthesis of Metallic and Bimetallic Sponges/Dendrites as Efficient Catalysts for 4-Nitrophenol Reduction. *Dalton Trans.* **2015**, *44*, 4215–4222. [CrossRef]
20. Zhou, L.; Xu, J.; Chen, C.; Wang, F.; Li, X. Synthesis of Fe, Co, and Mn Substituted AlPO-5 Molecular Sieves and Their Catalytic Activities in the Selective Oxidation of Cyclohexane. *J. Porous Mater.* **2008**, *15*, 7–12. [CrossRef]
21. Liu, G.; Wang, Z.; Jia, M.; Zou, X.; Zhu, X.; Zhang, W.; Jiang, D. Thermally Stable Amorphous Mesoporous Aluminophosphates with Controllable P/Al Ratio: Synthesis, Characterization, and Catalytic Performance for Selective O-Methylation of Catechol. *J. Phys. Chem. B* **2006**, *110*, 16953–16960. [CrossRef] [PubMed]
22. Gándara, F.; López-Arbeloa, F.; Ruiz-Hitzky, E.; Camblor, M.A. "Bottle-around-a-Ship" Confinement of High Loadings of Acridine Orange in New Aluminophosphate Crystalline Materials. *J. Mater. Chem.* **2006**, *16*, 1765–1771. [CrossRef]
23. Vaughan, D.E.W.; Yennawar, H.P.; Perrottat, A.J. Synthesis and Structure of an Aluminophosphate Built from 3-Rings. *Chem. Mater.* **2006**, *18*, 3611–3615. [CrossRef]
24. Hu, Y.; Navrotsky, A.; Chen, C.Y.; Davis, M.E. Thermochemical Study of the Relative Stability of Dense and Microporous Aluminophosphate Frameworks. *Chem. Mater.* **1995**, *7*, 1816–1823. [CrossRef]
25. Kumar, R.; Rajendiran, R.; Choudhary, H.K.; Naveen, N.K.; Balaiah, B.; Anupama, A.V.; Sahoo, B. Role of Pyrolysis Reaction Temperature and Heating-Rate in the Growth and Morphology of Carbon Nanostructures. *Nano-Struct. Nano-Objects* **2017**, *12*, 229–238. [CrossRef]
26. Kumar, R.; Anupama, A.V.; Kumaran, V.; Sahoo, B. Effect of Solvents on the Structure and Magnetic Properties of Pyrolysis Derived Carbon Globules Embedded with Iron/Iron Carbide Nanoparticles and Their Applications in Magnetorheological Fluids. *Nano-Struct. Nano-Objects* **2018**, *16*, 167–173. [CrossRef]

27. Kumar, R.; Sahoo, B. Carbon Nanotubes or Carbon Globules: Optimization of the Pyrolytic Synthesis Parameters and Study of the Magnetic Properties. *Nano-Struct. Nano-Objects* **2018**, *14*, 131–137. [CrossRef]

28. Kumar, R.; Sahoo, B. One-Step Pyrolytic Synthesis and Growth Mechanism of Core–Shell Type Fe/Fe₃C-Graphite Nanoparticles-Embedded Carbon Globules. *Nano-Struct. Nano-Objects* **2018**, *16*, 77–85. [CrossRef]

29. Choudhary, H.K.; Kumar, R.; Pawar, S.P.; Sundararaj, U.; Sahoo, B. Effect of Morphology and Role of Conductivity of Embedded Metallic Nanoparticles on Electromagnetic Interference Shielding of PVDF-Carbonaceous-Nanofiller Composites. *Carbon* **2020**, *164*, 357–368. [CrossRef]

30. Kumar, R.; Kumar, A.; Verma, N.; Khopkar, V.; Philip, R.; Sahoo, B. Ni Nanoparticles Coated with Nitrogen-Doped Carbon for Optical Limiting Applications. *ACS Appl. Nano Mater.* **2020**, *3*, 8618–8631. [CrossRef]

31. Kumar, R.; Choudhary, H.K.; Anupama, A.V.; Menon, A.V.; Pawar, S.P.; Bose, S.; Sahoo, B. Nitrogen Doping as a Fundamental Way to Enhance the EMI Shielding Behavior of Cobalt Particle-Embedded Carbonaceous Nanostructures. *New J. Chem.* **2019**, *43*, 5568–5580. [CrossRef]

32. Kumar, R.; Kumar, A.; Verma, N.; Anupama, A.V.; Philip, R.; Sahoo, B. Modulating Non-Linear Optical Absorption through Controlled Graphitization of Carbon Nanostructures Containing Fe₃C-Graphite Core-Shell Nanoparticles. *Carbon* **2019**, *153*, 545–556. [CrossRef]

33. Kumar, R.; Kumar, A.; Verma, N.; Philip, R.; Sahoo, B. Mechanistic Insights into the Optical Limiting Performance of Carbonaceous Nanomaterials Embedded with Core-Shell Type Graphite Encapsulated Co Nanoparticles. *Phys. Chem. Chem. Phys.* **2020**, *22*, 27224–27240. [CrossRef] [PubMed]

34. Kumar, R.; Kumar, A.; Verma, N.; Philip, R.; Sahoo, B. FeCoCr Alloy-Nanoparticle Embedded Bamboo-Type Carbon Nanotubes for Non-Linear Optical Limiting Application. *J. Alloys Compd.* **2020**, *849*, 156665. [CrossRef]

35. Yadav, A.; Kumar, R.; Choudhary, H.K.; Sahoo, B. Graphene-Oxide Coating for Corrosion Protection of Iron Particles in Saline Water. *Carbon* **2018**, *140*, 477–487. [CrossRef]

36. Yadav, A.; Kumar, R.; Sahoo, B. Graphene Oxide Coatings on Amino Acid Modified Fe Surfaces for Corrosion Inhibition. *ACS Appl. Nano Mater.* **2020**, *3*, 3540–3557. [CrossRef]

37. Yadav, A.; Kumar, R.; Pandey, U.P.; Sahoo, B. Role of Oxygen Functionalities of GO in Corrosion Protection of Metallic Fe. *Carbon* **2021**, *173*, 350–363. [CrossRef]

38. Kumar, R.; Manjunatha, M.; Anupama, A.V.; Ramesh, K.P.; Sahoo, B. Synthesis, Composition and Spin-Dynamics of FCC and HCP Phases of Pyrolysis Derived Co-Nanoparticles Embedded in Amorphous Carbon Matrix. *Ceram. Int.* **2019**, *45*, 19879–19887. [CrossRef]

39. Kumar, R.; Sahoo, B. Investigation of Disorder in Carbon Encapsulated Core-Shell Fe/Fe₃C Nanoparticles Synthesized by One-Step Pyrolysis. *Diam. Relat. Mater.* **2018**, *90*, 62–71. [CrossRef]

40. Choudhary, H.K.; Kumar, R.; Pawar, S.P.; Sundararaj, U.; Sahoo, B. Enhancing Absorption Dominated Microwave Shielding in Co@C-PVDF Nanocomposites through Improved Magnetization and Graphitization of the Co@C-Nanoparticles. *Phys. Chem. Chem. Phys.* **2019**, *21*, 15595–15608. [CrossRef]

41. Kumar, R.; Khan, M.A.; Anupama, A.V.; Krupanidhi, S.B.; Sahoo, B. Infrared Photodetectors Based on Multiwalled Carbon Nanotubes: Insights into the Effect of Nitrogen Doping. *Appl. Surf. Sci.* **2021**, *538*, 148187. [CrossRef]

42. Kumar, R.; Choudhary, H.K.; Pawar, S.P.; Bose, S.; Sahoo, B. Carbon Encapsulated Nanoscale Iron/Iron-Carbide/Graphite Particles for EMI Shielding and Microwave Absorption. *Phys. Chem. Chem. Phys.* **2017**, *19*, 23268–23279. [CrossRef] [PubMed]

43. Mahour, L.N.; Choudhary, H.K.; Kumar, R.; Anupama, A.V.; Sahoo, B. Structural, Optical and Mössbauer Spectroscopic Investigations on the Environment of Fe in Fe-Doped ZnO (Zn₁₋ₓFeₓO) Ceramics Synthesized by Solution Combustion Method. *Ceram. Int.* **2019**, *45*, 24625–24634. [CrossRef]

44. Mohapatra, S.K.; Sahoo, B.; Keune, W.; Selvam, P. Synthesis, Characterization and Catalytic Activity of Mesoporous Trivalent Iron Substituted Aluminophosphates. *Chem. Commun.* **2002**, *223*, 1466–1467. [CrossRef] [PubMed]

45. Anupama, A.V.; Kumar, R.; Choudhary, H.K.; Sahoo, B. Synthesis of Coral-Shaped Yttrium-Aluminium-Iron Garnets by Solution-Combustion Method. *Ceram. Int.* **2018**, *44*, 3024–3031. [CrossRef]

46. Choudhary, H.K.; Kumar, R.; Pawar, S.P.; Anupama, A.V.; Bose, S.; Sahoo, B. Effect of Coral-Shaped Yttrium Iron Garnet Particles on the EMI Shielding Behaviour of Yttrium Iron Garnet-Polyaniline-Wax Composites. *ChemistrySelect* **2018**, *3*, 2120–2130. [CrossRef]

47. Anupama, A.V.; Choudhary, H.K.; Kumar, R.; Kumaran, V.; Sahoo, B. Steady-Shear Response of Magnetorheological Fluid Containing Coral-Shaped Yttrium-Iron-Garnet Particles. *Mater. Res. Bull.* **2019**, *113*, 45–50. [CrossRef]

48. Khassin, A.A.; Yurieva, T.M.; Kaichev, V.V.; Bukhtiyarov, V.I.; Budneva, A.A.; Paukshtis, E.A.; Parmon, V.N. Metal–Support Interactions in Cobalt-Aluminum Co-Precipitated Catalysts: XPS and CO Adsorption Studies. *J. Mol. Catal. A Chem.* **2001**, *175*, 189–204. [CrossRef]

49. Khassin, A.A.; Yurieva, T.M.; Kustova, G.N.; Plyasova, L.M.; Itenberg, I.S.; Demeshkina, M.P.; Chermashentseva, G.K.; Anufrienko, V.F.; Zaikovskii, V.I.; Larina, T.V.; et al. Cobalt-Containing Catalysts Supported by Synthetic Zn- and Mg-Stevensites and Their Performance in the Fischer–Tropsch Synthesis. *J. Mol. Catal. A Chem.* **2001**, *168*, 209–224. [CrossRef]

50. Kungurova, O.A.; Khassin, A.A.; Cherepanova, S.V.; Saraev, A.A.; Kaichev, V.V.; Shtertser, N.V.; Chermashentseva, G.K.; Gerasimov, E.Y.; Paukshtis, E.A.; Vodyankina, O.V.; et al. δ-Alumina Supported Cobalt Catalysts Promoted by Ruthenium for Fischer-Tropsch Synthesis. *Appl. Catal. A Gen.* **2017**, *539*, 48–58. [CrossRef]

51. Grandjean, D.; Pelipenko, V.; Batyrev, E.D.; van den Heuvel, J.C.; Khassin, A.A.; Yurieva, T.M.; Weckhuysen, B.M. Dynamic Cu/Zn Interaction in SiO$_2$ Supported Methanol Synthesis Catalysts Unraveled by in Situ XAFS. *J. Phys. Chem. C* **2011**, *115*, 20175–20191. [CrossRef]

52. Kumar, R.; Kumar, S.; Chandrappa, S.G.; Goyal, N.; Yadav, A.; Ravishankar, N.; Prakash, A.S.; Sahoo, B. Nitrogen-Doped Carbon Nanostructures Embedded with Fe-Co-Cr Alloy Based Nanoparticles as Robust Electrocatalysts for Zn-Air Batteries. *J. Alloys Compd.* **2024**, *984*, 173862. [CrossRef]

53. Kumar, S.; Kumar, R.; Goyal, N.; Vazhayil, A.; Yadav, A.; Thomas, N.; Sahoo, B. N-Doped Carbon Nanotubes Nucleated through Cobalt Nanoparticles as Bifunctional Catalysts for Zinc–Air Batteries. *ACS Appl. Nano Mater.* **2024**, *7*, 7865–7882. [CrossRef]

54. Kumar, A.; Kumar, R.; Verma, N.; Anupama, A.V.; Choudhary, H.K.; Philip, R.; Sahoo, B. Effect of the Band Gap and the Defect States Present within Band Gap on the Non-Linear Optical Absorption Behaviour of Yttrium Aluminium Iron Garnets. *Opt. Mater.* **2020**, *108*, 110163. [CrossRef]

55. Choudhary, H.K.; Kumar, R.; Patangrao, S.; Sahoo, B. Role of Graphitization-Controlled Conductivity in Enhancing Absorption Dominated EMI Shielding Behavior of Pyrolysis-Derived Fe$_3$C@C-PVDF Nanocomposites. *Mater. Chem. Phys.* **2021**, *263*, 124429. [CrossRef]

56. Chrétien, M.N.; Heafey, E.; Scaiano, J.C. Reducing Adverse Effects from UV Sunscreens by Zeolite Encapsulation: Comparison of Oxybenzone in Solution and in Zeolites. *Photochem. Photobiol.* **2010**, *86*, 153–161. [CrossRef]

57. Jiménez, J.A. Optical Properties of Eu3+-Doped Aluminophosphate Glass with a High Concentration of Silver and Tin. *J. Inorg. Organomet. Polym. Mater.* **2017**, *27*, 372–379. [CrossRef]

58. Yang, L.; Kruse, B. Revised Kubelka—Munk Theory I. Theory. *J. Opt. Soc. Am.* **2004**, *21*, 1933–1941. [CrossRef] [PubMed]

59. Kokhanovsky, A.A. Physical Interpretation and Accuracy of the Kubelka-Munk Theory. *J. Phys. D Appl. Phys.* **2007**, *40*, 2210–2216. [CrossRef]

60. Tamon, H.; Ishizaka, H.; Yamamoto, T.; Suzuki, T. Preparation of Mesoporous Carbon by Freeze Drying. *Carbon* **1999**, *37*, 2049–2055. [CrossRef]

61. Saha, D.; Deng, S. Adsorption Equilibrium and Kinetics of CO$_2$, CH$_4$, N$_2$O, and NH$_3$ on Ordered Mesoporous Carbon. *J. Colloid Interface Sci.* **2010**, *345*, 402–409. [CrossRef] [PubMed]

62. Nivetha, R.; Asrami, M.R.; Kumar, R.; Sharma, S.; Jourshabani, M.; Kumar, R.D.; Ravichandran, S.; Lee, B.; Lee, Y.; Chung, J.S.; et al. Highly Immobilized Bimetallic Fe/M-N4 (M- Mg or Zn) Conductive Metal–Organic Frameworks on Nitrogen-Doped Porous Carbon for Efficient Electrocatalytic Hydrogen Evolution and Oxygen Reduction Reactions. *Small Struct.* **2024**, *5*, 2300355. [CrossRef]

63. Georgiou, E. Catalytic Carbon-Carbon Coupling and Reduction Using Crystalline Porous Solids for Sustainability and Environmental Applications. Doctoral Dissertation, University of Southampton, Southampton, UK, 2017.

64. Mohapatra, S.K.; Sonavane, S.U.; Jayaram, R.V.; Selvam, P. Heterogeneous Catalytic Transfer Hydrogenation of Aromatic Nitro and Carbonyl Compounds over Cobalt(II) Substituted Hexagonal Mesoporous Aluminophosphate Molecular Sieves. *Tetrahedron Lett.* **2002**, *43*, 8527–8529. [CrossRef]

65. Maharana, R.; Bhanu Prasad, V.V.; Roy, S.; Prasad, D.; Kumar, K.; Paik, P.; Hebalkar, N.; Shukla, A.; Bal, R. Synthesis of High Temperature Stable Carbon Coated Metal Nanoparticles in AlPO$_4$ Based Matrix in Situ in Oxidative Atmosphere. *J. Am. Ceram. Soc.* **2016**, *99*, 64–71. [CrossRef]

66. Shi, Q.-x.; Lv, R.-w.; Zhang, Z.-x.; Zhao, D.-f. Advances in Heterogeneous Catalytic Transfer Hydrogenation of Aromatic Nitro Compounds. In Proceedings of the 3rd International Conference on Functional Molecules Compounds, Dalian, China, 8–11 September 2005; pp. 54–58.

67. Mohapatra, S.K.; Sonavane, S.U.; Jayaram, R.V.; Selvam, P. Reductive Cleavage of Azo Dyes and Reduction of Nitroarenes over Trivalent Iron Incorporated Hexagonal Mesoporous Aluminophosphate Molecular Sieves. *Appl. Catal. B* **2003**, *46*, 155–163. [CrossRef]

68. Selvam, P.; Mohapatra, S.K.; Sonavane, S.U.; Jayaram, R.V. Chemo- and Regioselective Reduction of Nitroarenes, Carbonyls and Azo Dyes over Nickel-Incorporated Hexagonal Mesoporous Aluminophosphate Molecular Sieves. *Tetrahedron Lett.* **2004**, *45*, 2003–2007. [CrossRef]

69. Rout, L.; Kumar, A.; Dhaka, R.S.; Reddy, G.N.; Giri, S.; Dash, P. Bimetallic Au-Cu Alloy Nanoparticles on Reduced Graphene Oxide Support: Synthesis, Catalytic Activity and Investigation of Synergistic Effect by DFT Analysis. *Appl. Catal. A Gen.* **2017**, *538*, 107–122. [CrossRef]

70. Menumerov, E.; Hughes, R.A.; Golze, S.D.; Neal, R.D.; Demille, T.B.; Campanaro, J.C.; Kotesky, K.C.; Rouvimov, S.; Neretina, S. Identifying the True Catalyst in the Reduction of 4-Nitrophenol: A Case Study Showing the Effect of Leaching and Oxidative Etching Using Ag Catalysts. *ACS Catal.* **2018**, *8*, 8879–8888. [CrossRef]

71. Wunder, S.; Polzer, F.; Lu, Y.; Mei, Y.; Ballauff, M. Kinetic Analysis of Catalytic Reduction of 4-Nitrophenol by Metallic Nanoparticles Immobilized in Spherical Polyelectrolyte Brushes. *J. Phys. Chem. C* **2010**, *114*, 8814–8820. [CrossRef]

72. Kong, X.K.; Sun, Z.Y.; Chen, M.; Chen, C.L.; Chen, Q.W. Metal-Free Catalytic Reduction of 4-Nitrophenol to 4-Aminophenol by N-Doped Graphene. *Energy Env. Sci* **2013**, *6*, 3260–3266. [CrossRef]

73. Gao, L.; Li, R.; Sui, X.; Li, R.; Chen, C.; Chen, Q. Conversion of Chicken Feather Waste to N-Doped Carbon Nanotubes for the Catalytic Reduction of 4-Nitrophenol. *Environ. Sci. Technol.* **2014**, *48*, 10191–10197. [CrossRef] [PubMed]

74. Menumerov, E.; Hughes, R.A.; Neretina, S. Catalytic Reduction of 4-Nitrophenol: A Quantitative Assessment of the Role of Dissolved Oxygen in Determining the Induction Time. *Nano Lett.* **2016**, *16*, 7791–7797. [CrossRef] [PubMed]

75. Koklioti, M.A.; Skaltsas, T.; Sato, Y.; Suenaga, K.; Stergiou, A.; Tagmatarchis, N. Mechanistic Insights into the Photocatalytic Properties of Metal Nanocluster/Graphene Ensembles. Examining the Role of Visible Light in the Reduction of 4-Nitrophenol. *Nanoscale* **2017**, *9*, 9685–9692. [CrossRef] [PubMed]

76. Yang, T.Q.; Ning, T.Y.; Peng, B.; Shan, B.Q.; Zong, Y.X.; Hao, P.; Yuan, E.H.; Chen, Q.M.; Zhang, K. Interfacial Electron Transfer Promotes Photo-Catalytic Reduction of 4-Nitrophenol by Au/Ag_2O Nanoparticles Confined in Dendritic Mesoporous Silica Nanospheres. *Catal. Sci. Technol.* **2019**, *9*, 5786–5792. [CrossRef]

77. Ciganda, R.; Li, N.; Deraedt, C.; Gatard, S.; Zhao, P.; Salmon, L.; Hernández, R.; Ruiz, J.; Astruc, D. Gold Nanoparticles as Electron Reservoir Redox Catalysts for 4-Nitrophenol Reduction: A Strong Stereoelectronic Ligand Influence. *Chem. Commun.* **2014**, *50*, 10126–10129. [CrossRef] [PubMed]

78. Qian, J.; Yuan, A.; Yao, C.; Liu, J.; Li, B.; Xi, F.; Dong, X. Highly Efficient Photo-Reduction of p-Nitrophenol by Protonated Graphitic Carbon Nitride Nanosheets. *ChemCatChem* **2018**, *10*, 4747–4754. [CrossRef]

79. Miah, A.T.; Malakar, B.; Saikia, P. Gold over Ceria-Titania Mixed Oxides: Solar Light Induced Catalytic Activity for Nitrophenol Reduction. *Catal. Lett.* **2016**, *146*, 291–303. [CrossRef]

80. Bekena, F.T.; Abdullah, H.; Kuo, D.H.; Zeleke, M.A. Photocatalytic Reduction of 4-Nitrophenol Using Effective Hole Scavenger over Novel Mg-Doped Zn(O,S) Nanoparticles. *J. Ind. Eng. Chem.* **2019**, *78*, 116–124. [CrossRef]

81. Liu, X.; Zhao, L.; Lai, H.; Zhang, X.; Yi, Z. Highly Effective Degradation of P-Nitrophenol Over MoS_2 Under Visible Light Illumination. *Catal Lett.* **2017**, *147*, 2153–2159. [CrossRef]

82. Chen, Y.; Sun, F.; Huang, Z.; Chen, H.; Zhuang, Z.; Pan, Z.; Long, J.; Gu, F. Photochemical Fabrication of SnO_2 Dense Layers on Reduced Graphene Oxide Sheets for Application in Photocatalytic Degradation of P-Nitrophenol. *Appl. Catal. B* **2017**, *215*, 8–17. [CrossRef]

83. Sahu, K.; Singh, J.; Mohapatra, S. Catalytic Reduction of 4-Nitrophenol and Photocatalytic Degradation of Organic Pollutants in Water by Copper Oxide Nanosheets. *Opt. Mater.* **2019**, *93*, 58–69. [CrossRef]

84. Zhao, S.; Ma, H.; Wang, M.; Cao, C.; Xiong, J.; Xu, Y.; Yao, S. Study on the Mechanism of Photo-Degradation of p-Nitrophenol Exposed to 254 nm UV Light. *J. Hazard. Mater.* **2010**, *180*, 86–90. [CrossRef] [PubMed]

85. Zhao, Y.; Li, R.; Jiang, P.; Zhang, K.; Dong, Y.; Xie, W. Mechanistic Study of Catalytic Hydride Reduction of -NO_2 to -NH_2 Using Isotopic Solvent and Reducer: The Real Hydrogen Source. *J. Phys. Chem. C* **2019**, *123*, 15582–15588. [CrossRef]

86. Fountoulaki, S.; Daikopoulou, V.; Gkizis, P.L.; Tamiolakis, I.; Armatas, G.S.; Lykakis, I.N. Mechanistic Studies of the Reduction of Nitroarenes by $NaBH_4$ or Hydrosilanes Catalyzed by Supported Gold Nanoparticles. *ACS Catal.* **2014**, *4*, 3504–3511. [CrossRef]

87. Nemanashi, M.; Meijboom, R. Synthesis and Characterization of Cu, Ag and Au Dendrimer-Encapsulated Nanoparticles and Their Application in the Reduction of 4-Nitrophenol to 4-Aminophenol. *J. Colloid Interface Sci.* **2013**, *389*, 260–267. [CrossRef] [PubMed]

88. Wunder, S.; Lu, Y.; Albrecht, M.; Ballauff, M. Catalytic Activity of Faceted Gold Nanoparticles Studied by a Model Reaction: Evidence for Substrate-Induced Surface Restructuring. *ACS Catal.* **2011**, *1*, 908–916. [CrossRef]

89. Morales, M.V.; Rocha, M.; Freire, C.; Asedegbega-Nieto, E.; Gallegos-Suarez, E.; Rodríguez-Ramos, I.; Guerrero-Ruiz, A. Development of Highly Efficient Cu versus Pd Catalysts Supported on Graphitic Carbon Materials for the Reduction of 4-Nitrophenol to 4-Aminophenol at Room Temperature. *Carbon* **2017**, *111*, 150–161. [CrossRef]